energies

MDPI

Article

Steel Hydrogen-Induced Degradation Diagnostics for Turbo Aggregated Rotor Shaft Repair Technologies

Alexander I. Balitskii [1,2,*], Valerii O. Kolesnikov [1,3], Maria R. Havrilyuk [1], Valentina O. Balitska [4], Igor V. Ripey [5], Marcin A. Królikowski [2] and Tomasz K. Pudlo [2]

[1] Department of Strength of the Materials and Structures in Hydrogen-Containing Environments, Karpenko Physico-Mechanical Institute, National Academy of Sciences of Ukraine, 5 Naukova Str., 79601 Lviv, Ukraine; kolesnikov197612@gmail.com (V.O.K.); gavriluk@ipm.lviv.ua (M.R.H.)
[2] Department of Mechanical Engineering and Mechatronics, West Pomeranian University of Technology in Szczecin, 19 Piastow Av., 70-310 Szczecin, Poland; marcin.krolikowski@zut.edu.pl (M.A.K.); pudlo.tomasz95@gmail.com (T.K.P.)
[3] Department of Professional Education, Educational and Research Institute of Technology and Commerce, Restaurant and Tourist Business, Luhansk Taras Shevchenko National University, 3 Ivan Bank St., 36003 Poltava, Ukraine
[4] Department of Physics and Chemistry of Combustion, Lviv State University of Life Safety, 35 Kleparivska, 79000 Lviv, Ukraine; vbalitska@yahoo.com
[5] Service Companies Galremenergo, PJSC "DTEK Zakhidenergo", 15 Kozelnytska Street, 79026 Lviv, Ukraine; ihor_techdiagnosis@ukr.net
* Correspondence: abalicki@zut.edu.pl or balitski@ipm.lviv.ua

Abstract

Rotor equipment material samples with varying degrees of degradation during long-term operation are characterized by lower (up to 17%) corrosion and hydrogen resistance compared to the initial state. The scheme of redistribution of carbides in structural components in the initial state and after long-term operation is presented. The schemes of the turning rotor shaft are visualized, while taking the microstructure features into account. During long-term service, the properties of steels are affected by changes in the parameters of structural components caused by the action of a hydrogen-containing environment. Based on the experimental data, the regression equation and approximation probability R^2 value describing the change in the electrochemical parameters of 38KhN3MFA rotor steel samples after 200, 225, 250, and 350 thousand hours of operation were obtained. During machining, an increase in hydrogen content was recorded in the chips, especially from degraded areas of the rotor shaft (up to 7.94 ppm), while in undegraded zones, it ranged from 2.1 to 4.4 ppm. A higher hydrogen concentration was correlated with increased surface roughness. The use of LCLs improved surface quality by 1.5 times compared to LCL_p. Dispersion caused by degradation contributed to hydrogen accumulation and changed the nature of material destruction. After repair, the rotors demonstrated stable operation for over 25 thousand hours, with no reappearance of critical defects observed during scheduled inspections.

Keywords: degradation; 38KhN3MFA rotor steel; corrosion resistance; rotor shaft; power equipment; electrochemical studies; hydrogen charging; turbo aggregate rotor shaft; machining; hydrogen accumulation; steel structural components; hydrogen diffusion; screening anions; computer vision methods

Received: 9 July 2025
Revised: 31 July 2025
Accepted: 13 August 2025
Published: 16 August 2025

Citation: Balitskii, A.I.; Kolesnikov, V.O.; Havrilyuk, M.R.; Balitska, V.O.; Ripey, I.V.; Królikowski, M.A.; Pudlo, T.K. Steel Hydrogen-Induced Degradation Diagnostics for Turbo Aggregated Rotor Shaft Repair Technologies. *Energies* **2025**, *18*, 4368. https://doi.org/10.3390/en18164368

1. Introduction

One of the most critical parts of a turbine unit cooled by hydrogen gas is the rotor shaft of the turbogenerator. The weight of a solid or welded rotor can reach 160 tunes with a

length of 11 m. The rotor is made from 25Kh1M1FA, 30Kh3MVFA, and 38KhN3MFA steels. The complex effects of hydrogen-containing media, temperature changes, and loads cause changes in physical and mechanical properties in the surface and subsurface layers of the rotor shaft (degradation) [1–6], and changes in a number of operational factors accelerate degradation processes. Rotor replacement is extremely rare. The service life of these unique parts is extended during scheduled or emergency repairs by surface machining of damaged rotor surfaces using environmentally friendly lubricating and cooling fluids, followed by sealing. Therefore, studying the patterns of changes in the physical and mechanical properties of these steels for power machine building during long-term operation is an urgent scientific task.

The novelty of this work is the development of a diagnostic approach based on chip analysis for detecting hydrogen-induced degradation in 38KhN3MFA rotor shafts. A correlation is established between hydrogen content in chips and surface roughness as indicators of material damage. Regression equations describing electrochemical parameter degradation over long-term service (200,000–350,000 h) are proposed. Additionally, a novel repair methodology is evaluated using eco-friendly lubricating cooling liquids that mitigate hydrogen embrittlement during machining and enhance surface quality. These findings contribute to practical rotor life extension and structural safety in hydrogen-cooled turbine systems.

The generalized scheme of the life cycle of power equipment (Figure 1a) shows that at the third stage, its failure is accelerated due to aging. In order to prevent it, it is necessary to focus on clarifying the mechanisms of degradation processes accompanied by microstructural changes [7,8]. One of the possible schemes of such a phenomenon (Figure 1b) is the stage of micropore formation and enlargement. The properties of the studied steels are significantly affected by changes in the proportions of carbides, nitrides, and intermetallic content [9–11].

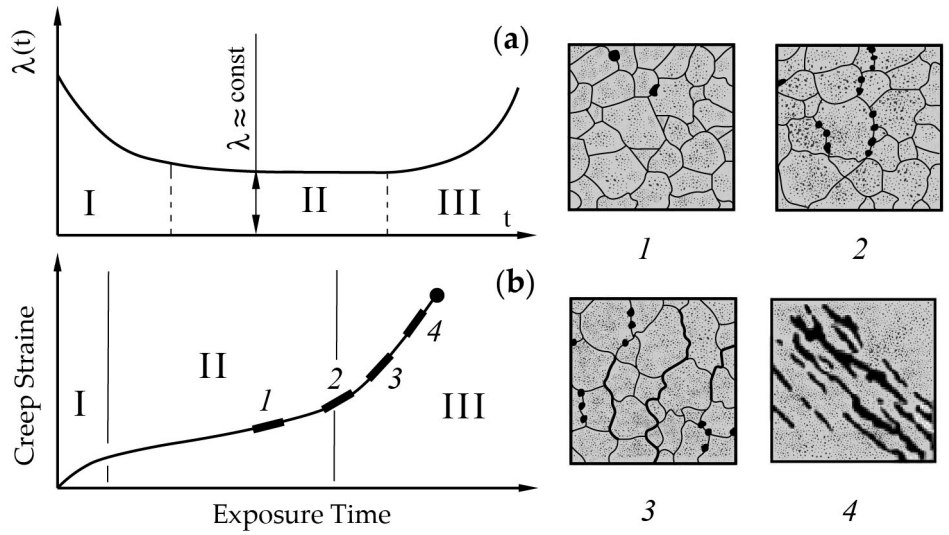

Figure 1. Life cycle change curve of power equipment. λ (**a**): failure rate; t (**a**)—time. Ex T (**b**)—exposure time. I—the period of commissioning; II—the period of normal operation; III—the period of aging, degradation, and failure (**a**) [1]. I—stage; II—stage; III—stage (**b**). 1—isolated cavities, 2—approximate cavities, 3—macrocracks, 4—formation and propagation of macrocracks [7].

During long-term operation, hydrogen has a significant effect on the properties of steels for power engineering, which at low concentrations can lead to plasticization of the metal matrix [12], and with an increase in its content and an increase in concentration in local volumes, it contributes to the "embrittlement" of this matrix, the initiation and

propagation of cracks [13–19]. In some cases, this leads to catastrophic consequences during the operation of power equipment in turbine halls [20–24].

Hydrogen vapor affects the surface and subsurface layers of the turbine rotor shaft. Unlike the turbine generator rotor shaft, temperatures on the surface of turbine rotor shafts vary within a fairly wide range along the length, which affects the intensity of changes in mechanical properties. On the high-pressure rotor shaft of the K-200-130 turbine, the temperature in the flow area is about 510 °C and closer to the first stage; it decreases to 280 °C near the last stage. On the HPR shaft of the K-1000-60/3000 turbine in the flow section, the temperature near the first stage is about 265 °C and 155 °C near the last five stages. In the area of the end seals, the temperatures are even lower, and in the area of the order bearings, temperatures are 55–60 °C.

During long-term operation, the hardness on the shaft surface decreased from 290 to 250 HB [25], the amount of cementite decreased from 87% to 62%, and the proportion of free ferrite increased from 5% to 20%. In degraded areas of the rotor shaft, it is necessary to carry out repair work related to machining [26–29]. During this process, lubricating coolants are used, which also perform inhibitory functions to prevent the development and spread of corrosion processes [30,31]. It is proposed to use environmentally friendly coolants containing sunflower or rapeseed oil [32–34].

The aim of this work is to compare the electrochemical parameters of the experimental samples in the form of chips (taken during the process of turning or drilling) from the rotor surfaces in the initial state and during long-term operation of 38KhN3MFA steel, analyze the data indicating changes in the physical and chemical properties of the material during long-term operation, and relate these factors to the morphology of the studied chips.

2. Materials and Methods

The samples of 38Kh3MFA steel were studied in the initial state (witness samples) and those taken during long-term operation in contact with technological hydrogen-containing media (mainly after 200, 250, and up to 350 thousand hours). The samples of chips from the supply material and those obtained during machining of the shaft after 200, 225, and 250 thousand hours of operation were studied. The microstructure of the studied samples is characterized by the presence of bainite and ferrite. Bainite contains a mixture of carbon-saturated ferrite and iron carbide. The grain size in the shaft steel after heat treatment is within 25. . .35 μm.

The corrosion potential (E_{cor}) and the corrosion current density (I_{cor}) were investigated using an EG&INSTRUMETS potentiostat (Model N 362) at a potential sweep rate of 10 mV/min. A standard three-electrode electrochemical cell with a silver chloride reference electrode was used, which was connected to the test electrode using an electrolytic bridge and a Haber–Luggin capillary, as well as an auxiliary platinum electrode. The polarization curves were obtained on samples with a diameter of 11.3 mm, which were pre-pressed into PTFE. The influence of samples of lubricating and cooling fluids (LCF) based on sunflower (LCF_s), rapeseed (LCF_r), and petroleum oil (LCF_p) was studied. Since the cooling circuit of turbine generators may contain distilled water condensate (pH 5.9) in addition to hydrogen, the corresponding comparative tests were carried out.

Figure 2 presents a flowchart of the technological process for rotor shaft diagnostics, which includes the main technological operations, including chip sampling.

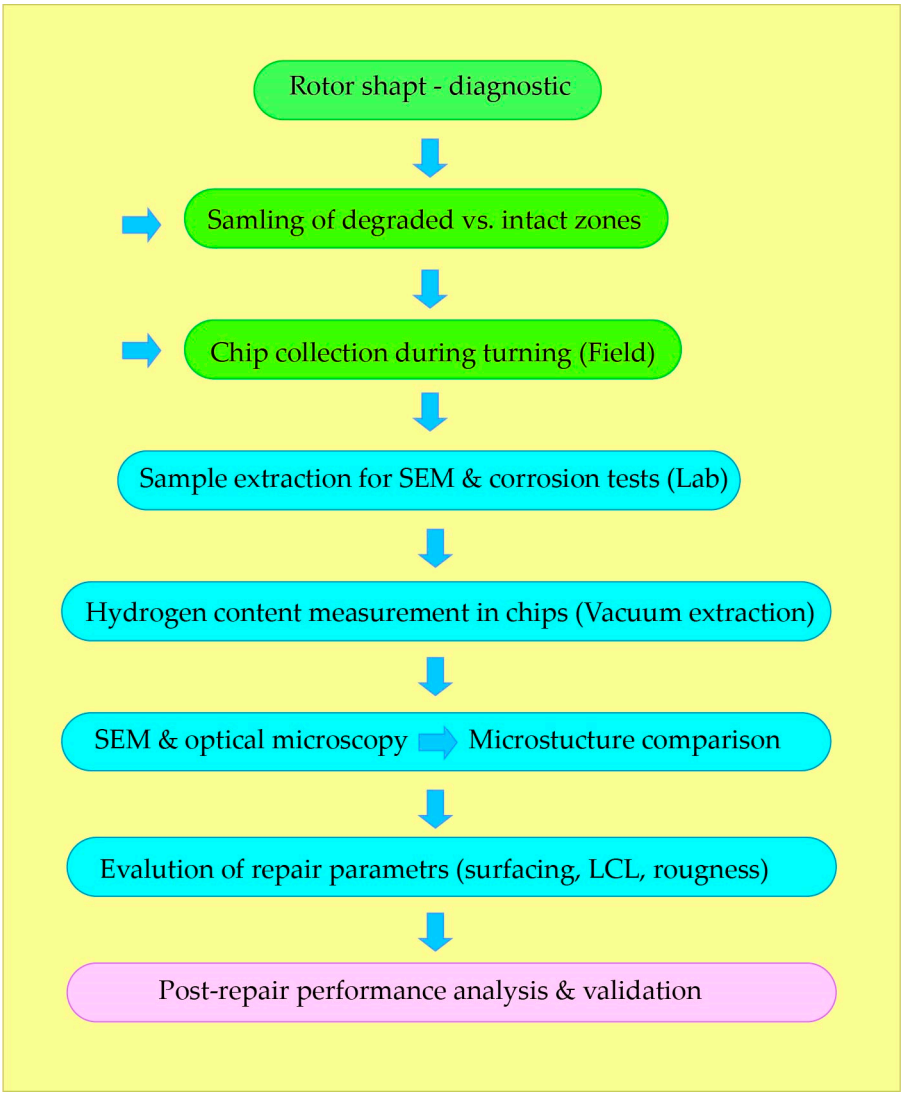

Figure 2. Flowchart of the rotor shaft diagnostics process.

3. Results

3.1. Structural-Phase Approaches and Reflections

This research was based on the concept that during long-term operation, due to the complex action of factors (mainly hydrogen), structural changes occur in the surface and subsurface layers of the turbine unit shaft.

Metallographic studies of the shaft surfaces of a number of turbine units have recorded changes in the orientation of ferrite and cementite inclusions [25], indicating the course of deformation processes due to the action of hydrogen gas [35]. Degradation processes on the surface of the turbine unit rotor shaft cause carbides to move from the central part of the grain to the boundaries (Figure 3a,b). During long-term operation, there is a gradual accumulation of hydrogen in the structural components: the cement component is capable of accumulating 10. . .12 ppm, pearlite 7–8 ppm, and ferrite 1–2 ppm [36] (Figure 3c,d). Taking in to account that structural components (this is most true for carbides) accumulate hydrogen, the probability of brittle fracture increases and the conditions of fracture during machining change.

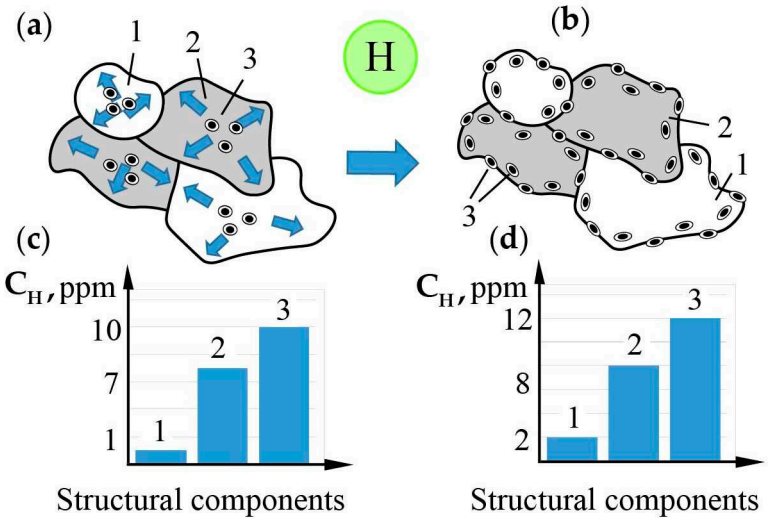

Figure 3. Scheme of redistribution of carbides in structural components: conditionally initial state (**a**); after long-term operation (**b**); diagram of the amount of hydrogen in structural components (**c**,**d**). Designations: 1—ferrite; 2—pearlite; 3—carbides.

An increase in temperature changes the quantitative composition of alloying elements (increases the concentration of Cr, Mo, and Mn, and decreases Fe without changing V) in the complex carbide $M_{23}C_6$ [37], and is accompanied by an increase in their size, which affects the performance properties of the rotor steel.

The quality of machining is significantly influenced by structural and phase components (in addition to carbides, this is sulfide (MnS), which at elevated temperatures during long-term operation of power equipment [36,37] concentrates along grain boundaries and has an elongated shape). In waterlogged samples, cracks appear along the elongated inclusions [38], and the presence of sulfur (including in the form of MnS inclusions (their size, shape, and distribution) also affects the quality of machining and the nature of fracture [39–48].

Figure 4 shows a generalized schematic diagram illustrating the microstructure of 38Kh3NMFA rotor steel with a ferrite–pearlite base and the mechanisms of interaction with hydrogen. The diagram shows the paths of hydrogen (H) diffusion through the matrix, reversible and irreversible traps, as well as local areas of embrittlement. Ferrite (light yellow) and pearlite (light gray) form the basis of the microstructure. Dislocations and grain boundaries act as reversible traps capable of releasing hydrogen under mechanical stress. Complex carbides of the Cr/Mo/Fe_3C type, located at grain boundaries or in the matrix, function as irreversible traps, accumulating hydrogen and promoting the formation of microcracks. Accumulated hydrogen at grain boundaries and in carbide phases can initiate intergranular or localized brittle fracture, which is particularly critical for turbogenerator rotors operating under hydrogen cooling conditions.

Complex carbides in 38KhN3MFA steel most commonly form at grain boundaries and phase boundaries (ferrite–pearlite), and less frequently within grains. Their location directly affects the ability to accumulate hydrogen and the susceptibility to degradation under service conditions.

In steels with a ferrite–pearlite structure, such as 38KhN3MFA, hydrogen saturation can indeed lead to the formation of the following:

- new dislocations;
- new or displaced grain boundaries;
- substructures (subgrains);
- zones of local rearrangement;

- in some cases, heterogeneous formation of new grains (structure reformation).

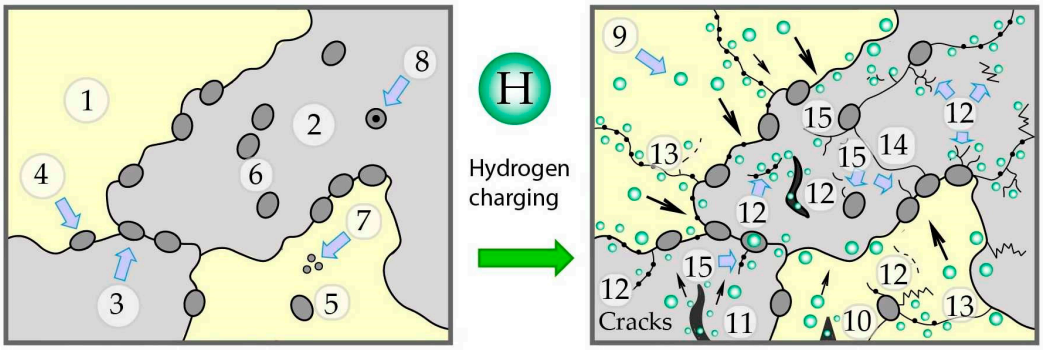

Figure 4. Generalized schematic diagram illustrating the microstructure of 38KhN3MFA rotor steel with a ferrite–pearlite metallic matrix: (**a**) before hydrogenation; (**b**) after hydrogen charging: 1—ferrite; 2—pearlite; 3—carbides ($M_{23}C_6$, M_7C_3, Fe_3C); 4—carbides (Cr/Mo/Fe_3C); 5—dispersed carbides (Mo_2C, VC); 6—manganese sulfides (MnS); 7—intermetallic phases; 8—various inclusions (nitrides, phosphides, oxides, etc.); 9—hydrogen; 10—surface crack induced by hydrogen; 11—surface-initiated crack propagating into the material; 12—crack; 13—newly formed interface boundary in ferrite; 14—newly formed interface boundary in pearlite; 15—microcrack formation due to stress concentration near structural constituents such as carbides and others. The arrows indicate the conditional distribution of hydrogen in the structural components.

3.2. Effect of Structural-Phase Composition Under Conditions of Gradual Hydrogen Charging on Machining

Taking into account the above features of structural and phase changes, the following technological operations are proposed for machining (Figure 5a,b). Slowly gradual feeding (1) of the cutter (2) into the chip formation zone (3) and formation of a new surface (4) during machining of the rotor shaft (5) after prolonged operation. The metal matrix contains carbides, sulphides, and intermetallic content (6), which are stress concentrators and contribute to the formation of cracks (7, 7*), given the tendency for branched cracks to form smaller chips. The size and distribution of carbides and intermetallic contents affect the formation of growth (8, 8*—smaller growth). An increase in the build-up between the cutter and the workpiece increases the surface roughness. During long-term operation, the metal matrix, carbides, sulfides, and intermetallic contents are hydrogen charging, which is accompanied by a change in their location in the grains. Hydrogen between the inclusion and the metal matrix affects the stress field and contributes to the accelerated destruction of the subsurface layers during machining. If the main frontal angle of the cutter is negative, a surface nanostructure with a high density of dislocations and residual compressive stresses is formed during turning [49], and the surface nanostructure blocks the penetration of hydrogen into the matrix material [50–52].

It was recorded that the amount of cementite in the microstructure of the shaft decreased from 87% to 62% over 250 thousand hours of operation, and the proportion of free ferrite increased from 5% to 20% [22].

It was found that in the degraded material, the content of alloying elements in the carbide phase increases, and in the solid solution of the metal matrix, the content decreases compared to the initial state. The intensification of diffusion processes increases the concentration of carbide-forming elements: along grain boundaries and in carbides. In special carbides, an increase in the content of chromium and vanadium was recorded: 1.05–1.65 times, and for molybdenum, 2.22–2.85 times [22].

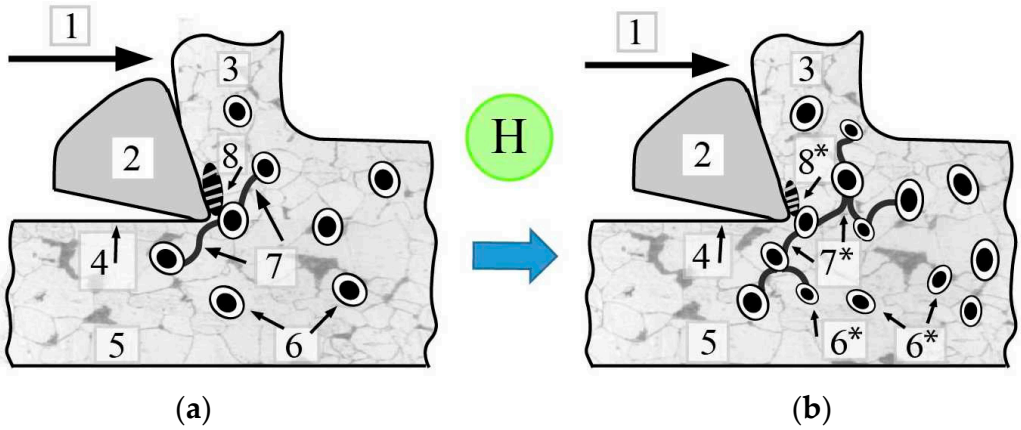

Figure 5. Scheme of rotor shaft turning: conditionally initial condition (**a**); after long-term operation (**b**). Designations: 1—direction of turning; 2—cutter; 3—chips; 4—machining surface; 5—rotor shaft; 6—carbides, sulfides, and intermetallic content; 7—cracks; 8—growth between the cutter and the rotor shaft (6*, 7*, 8*—after hydrogen charging).

Microstructure Figure 6a—zone near the rotor shaft bearing (hydrogen environment—above)

Structure characteristics:

The microstructure is a finely dispersed ferrite–pearlite mixture with a uniform distribution of phases. Pearlite is presented in the form of small, isotropically arranged columns/plates, and ferrite is presented in the form of light islands with an almost uniform distribution.

Micromorphology:

The structure is dense, without a pronounced deformation texture. Fine grains are visible, which indicates diffusion saturation with hydrogen, but without significant destruction.

Interpretation:

The zone was probably under conditions of moderate hydrogen action, which caused the dissolution of pearlite columns, but without the formation of cracks. Hydrogen acted mainly on the grain boundaries, causing deformation relaxation.

Microstructure Figure 6b—zone near the trunnion (hub) (intensive contact with hydrogen)

Characteristics of the structure:

A significant blurring of the boundaries of the ferrite–pearlite structure is observed, with a chaotic arrangement of elongated pearlite columns. The pearlite zones are disorganized, and the structure looks more inhomogeneous and elongated in the stress directions.

Micromorphology:

Signs of local deformation are observed, with oriented structures and probable formation of hydrogen-induced defects (micropores, unstable grain boundaries). This indicates intensive interaction with hydrogen.

Interpretation:

The microstructure indicates an active hydrogen influence, probable formation of hydrogen traps in carbides, and displacement of phase boundaries, presumably a degradation zone. The trunnion was in contact with hydrogen at high temperatures, which caused localized plasticity and inhomogeneous relaxation of the phases.

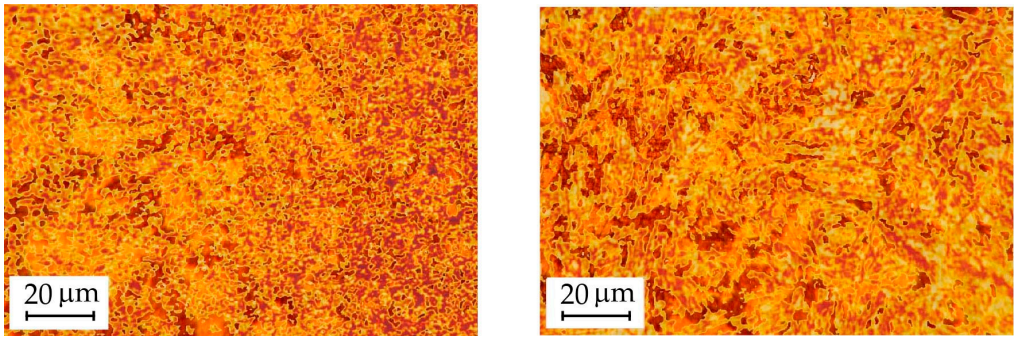

(**a**) (**b**)

Figure 6. Microstructures of the turbine unit rotor shaft surface 38KhN3MFA after prolonged operation in contact with hydrogen: near the bearing seal (**a**) and near the bearing hub (**b**).

Chips are an identifier of degradation processes in the surface and subsurface layers of a rotor shaft or other equipment. Figure 7a shows a chip with a microrelief that is typical of the initial condition, and Figure 7b shows a chip with a different microrelief appearance. It has a more complex character, which is probably formed as a result of a complex effect of factors, one of which is the effect of hydrogen.

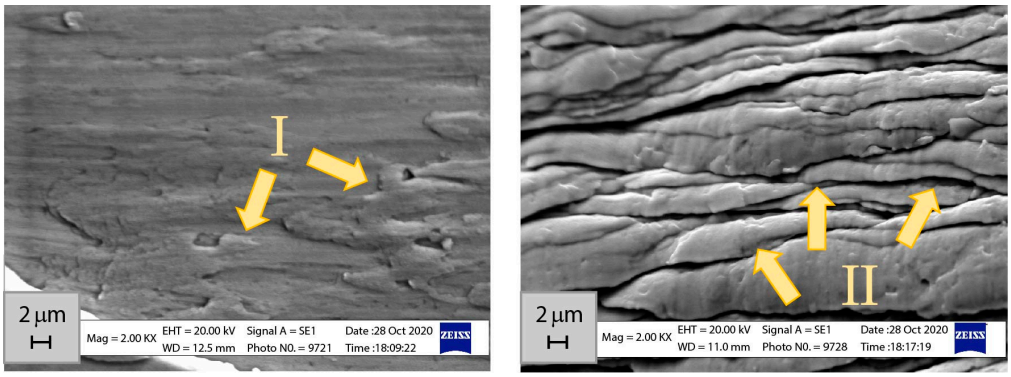

(**a**) (**b**)

Figure 7. Appearance of the chips: conditionally initial state (**a**) and from the degraded area (**b**).

Arrows I indicate (Figure 5a) the stepped microrelief of the chips. Arrows II indicate (Figure 5b) the presence of cracks that could have been formed as a result of the impact of the hydrogen-containing medium on the rotor shaft metal. The deformed surface has a roughly petal-like appearance, which may indicate the occurrence of intense deformation processes in the degraded surface during chip formation under machining conditions. Figures 8 and 9 show the visualization of the chip surface profile. For the chips (Figure 8a,b) which were formed from the initial state of the material, most of the surface has a microrelief in the range of −25–+25 conventional units, i.e., arbitrary height units calibrated within the profilometry software, and only in the right part of the images, there are those whose height peaks in the range of +15–+30 conventional units.

For the degraded surface (Figure 9b), there are a greater number of peaks (peak heights in the range of +25–+50 conventional units) than for the previous case. Also, low depressions with a depth of up to −50 conventional units are characteristic.

The amount of hydrogen recorded in the chips from the initial state (Figure 10a) is 0.87 ppm, while in the chips from the degraded area, it reaches 7.24 ppm.

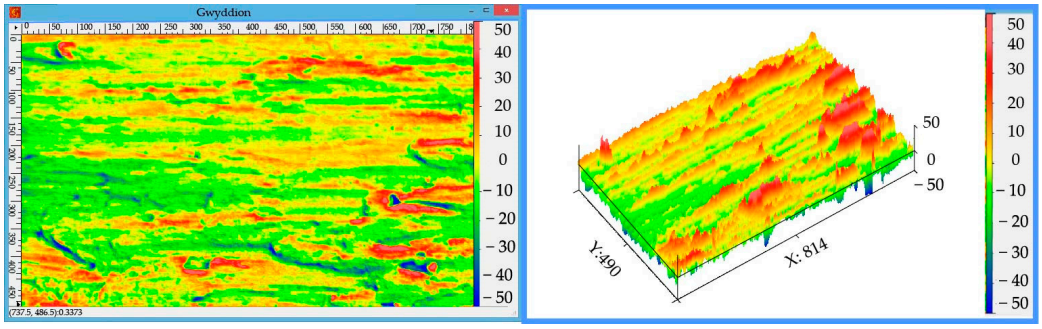

(**a**) (**b**)

Figure 8. Two-dimensional (**a**) and three-dimensional (**b**) reconstruction of the chip area presented in Figure 7a.

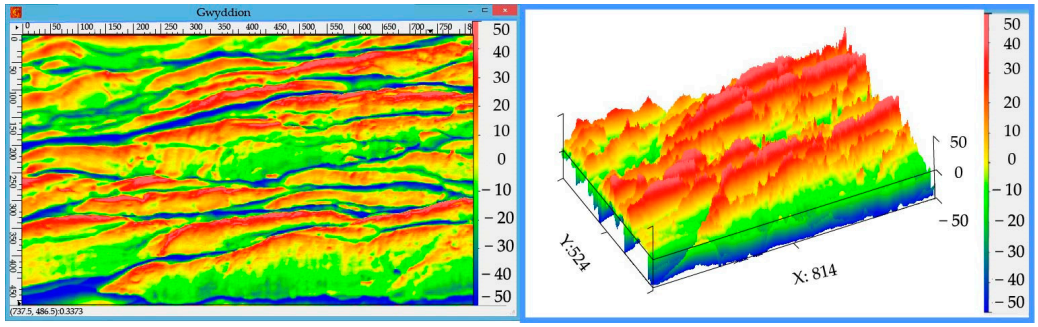

(**a**) (**b**)

Figure 9. Two-dimensional (**a**) and three-dimensional (**b**) reconstruction of the chip area presented in Figure 7b.

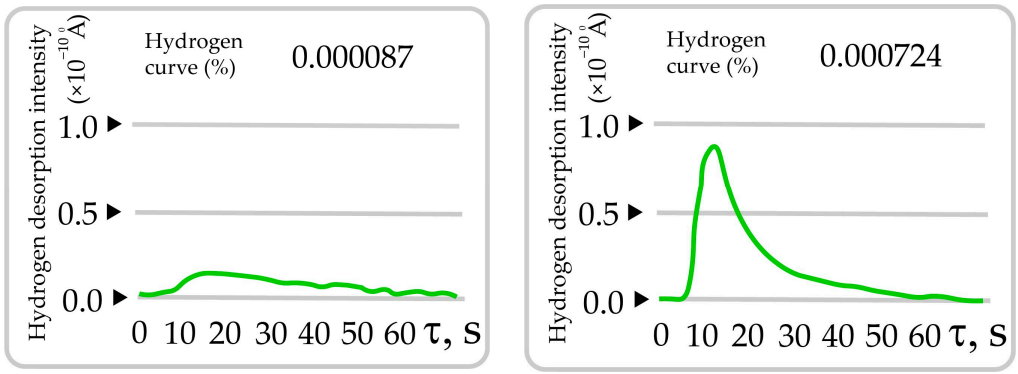

(**a**) (**b**)

Figure 10. Amount of hydrogen in the chips (**a**,**b**). Initial conditional state (**a**). From degradation chips (**b**).

3.3. Electrochemical Investigation

The analysis of the change in the corrosion potential of steels in different coolants revealed that it has a similar character. The value of the corrosion current density for 38KhN3MFA steel depends on the nature of the coolant base and increases in the following sequence: sunflower < rapeseed < oil (petroleum) (Table 1):

For material samples cut from sections of power equipment shafts with different degrees of degradation and different operating times, the corrosion resistance is 8. . .17% lower than that of steels in their original state.

To determine the ability of the coolant to protect the surface of machined parts from corrosion, as well as to determine the difference in electrochemical parameters for chips formed after their removal from the degraded section of the shaft, electrochemical studies

of polished samples in coolant and mineral water were performed. The effect of coolant on the rate of electrode processes is shown in Figure 11.

The nature of the curves for 38KhN3MFA steel (Figure 11) indicates the anodic nature of electrode processes. A stably passive region in the anode section of the polarization curves is observed for 38KhN3MFA only in the LCL_r. This indicates the formation of a continuous corrosion-resistant film on this steel in the indicated media.

Table 1. Electrochemical parameters of steel.

Environment	i_{cor}, $\cdot 10^4$ mA/cm^2	E_{cor}, mV	i_{cor}, $\cdot 10^4$ mA/cm^2	E_{cor}, mV	i_{cor}, $\cdot 10^4$ mA/cm^2	E_{cor}, mV	i_{cor}, $\cdot 10^4$ mA/cm^2	E_{cor}, mV
1	2	3	4	5	6	7	8	9
LCL_s	1.70 (100%)	−175	1.83 (8.12%)	−174	1.88 (10.61%)	−172	1.96 (15.44%)	−169
LCL_r	2.14 (100%)	−179	2.31 (8.27%)	−178	2.37 (10.94%)	−176	2.47 (15.77%)	−173
LCL_p	6.03 (100%)	−187	6.59 (9.35%)	−186	6.71 (11.33%)	−184	7.01 (16.39%)	−181
Water	16.02 (100%)	−325	17.62 (10.0%)	−324	18.03 (12.57%)	−322	18.78 (17.28%)	−319

1, 2, 3—output state; 4, 5—200 thousand hours of exploitation; 6, 7—225 thousand hours of exploitation; 8, 9—250 thousand hours of exploitation.

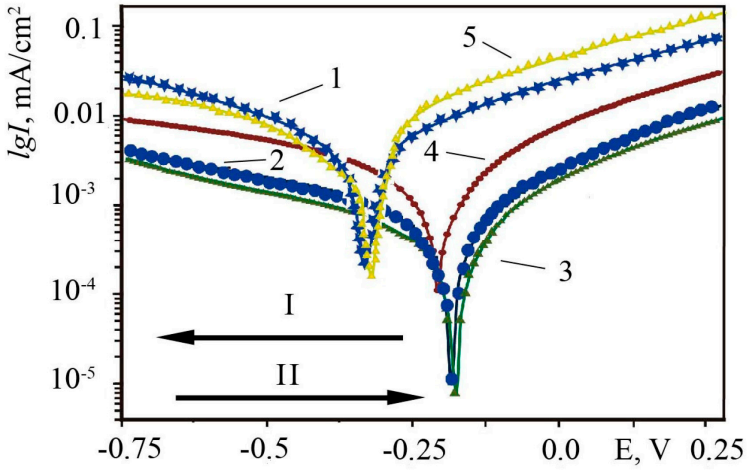

Figure 11. Polarization curves of the 38KhN3MFA steel obtained on the samples (conditional initial state): 1—water, 2—LCL_r, 3—LCL_s, 4—LCL_p, 5—water (after operation, 250 thousand hours). Conditionally initial state (I) and from the degraded area—operational condition (II).

Figure 12 shows the regression curves of the change in the i_{cor} corrosion current density obtained on samples exposed to different operating times in the media.

Regression analysis was performed (Table 2); a,b—coefficients; *p*-value for coefficients (especially ln(x)). If $p < 0.05$, this is considered statistically significant. CI denotes the confidence interval limits.

Regression analysis of the corrosion current density over time shows a strong logarithmic dependence ($R^2 > 0.81$ for all environments), with statistically significant slopes ($p < 0.05$). The increase in ln(i_{or}p) is most pronounced in distilled water, while the effect is minimal in LCLs. Confidence intervals for the slope coefficients confirm the reliability of these trends.

Table 2. Regression analysis results.

Environment	a (Slope)	b (Intercept)	R^2	*p*-Value	CI (a)
LCL_s	0.0752	1.8222	0.8886	0.012	(0.03–0.12)
LCL_r	0.0923	2.3	0.8817	0.015	(0.04–0.14)
LCL_p	0.2368	6.5562	0.8105	0.030	(0.09–0.39)
Water	0.6654	17.543	0.8655	0.010	(0.32–1.01)

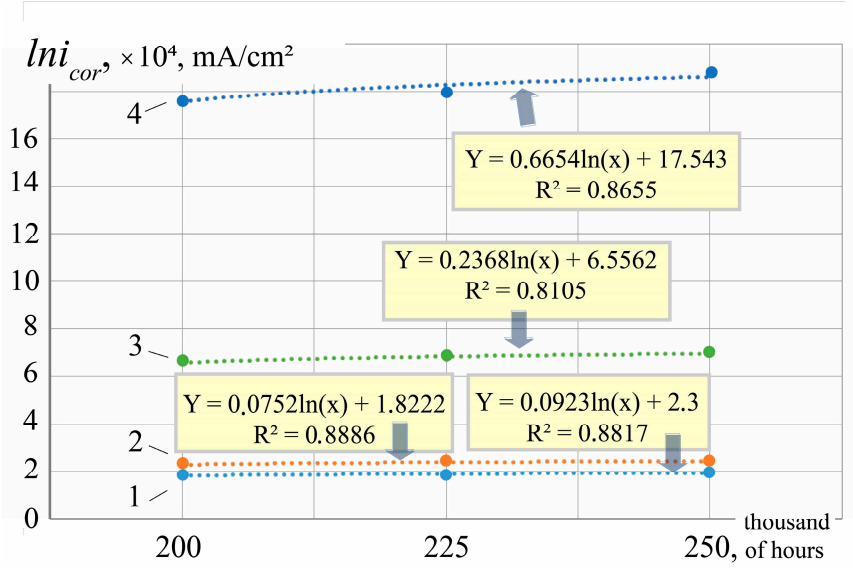

Figure 12. Regression curves of changes in the corrosion current density (i_{cor}) obtained on the samples exposed during different operation times in the following media: 1—water, 2—LCL_r, 3—LCL_s, 4—LCL_p.

Roughness values for the samples (Rz) (after machining): (conditionally initial condition/degraded after 200 thousand hours of operation): 37.08/57.47 (dry cutting); 5.01/7.11 (with water); 6.36/8.77 R_{zp}; 4.43/5.71 R_{zs}.

Our research shows that the concentration of hydrogen in the coolant is higher in chips made on an oil basis (petroleum) (7.86 ppm), and lower for chips made on a sunflower oil basis (7.22 ppm). Therefore, it is possible that the destructive effect of hydrogen on coolant under such technological conditions will be lower.

During machining, an increase in the amount of hydrogen in the chips formed both during machining [34] and from degraded areas of the rotor shaft was recorded. It was recorded during the processing of the amount of hydrogen (6.84. . .7.12 ppm), during the processing of the areas on the border with the degraded ones, and during processing of the most damaged areas (7.12. . .7.94 ppm). In the undegraded areas of the rotor shaft, the recorded hydrogen concentration ranged from 2.1 to 4.4 ppm. The surface quality of steel samples when honed with LCL_s improves almost 1.5 times compared to LCL_p and shows the prospects of using vegetable oil for LCLS. It should also be noted that an increase in the maximum recorded hydrogen concentration in the chips coincides with an increase in roughness. This may indicate that there is a range within which the effect of hydrogen from the LCL, together with the gradual hydrogen charging of the structural components of steel, provides optimal values of roughness during machining of the turbine generator rotor shaft. Increasing the degree of dispersion (including during degradation processes) in the studied areas led to an increase in the concentration of hydrogen, and, accordingly, to a change in the intensity and nature of destruction during machining, which is the main procedure affected by crack initiation and electric erosion rotor area repair technology.

4. Discussion

4.1. Common Provisions

Hydrogen can significantly affect the properties of steel parts that are exposed to hydrogen-containing environments for a long time [53–67]. Therefore, to study this problem, we can refer to many studies that may be even indirectly related.

In [57], to study the changes in the hydrogen embrittlement (HE) of CLAM steel during thermal aging, samples were kept at 550 °C and 600 °C for up to 5000 h. The evolution of the microstructure was studied: sub granules, $M_{23}C_6$ carbides, MX carbonitrides, and Laves phases. It has been found that the resistance to VC first increases and then decreases with increasing aging duration. The mechanisms of such changes are explained through the orientational bonds between the secretions and the matrix.

The influence of microstructure and reversed austenite (RA) on hydrogen embrittlement (HE) was studied in NiCrMoV/Nb high-strength steel subjected to three heat treatments. Quenched and tempered (QT) steel showed the best HE resistance due to low hydrogen diffusivity and high apparent hydrogen concentration. TDS analysis revealed RA has a trapping energy of 32.5 kJ/mol. However, the QLT steel, with more RA, showed higher HE susceptibility, indicating RA reduces HE resistance [59].

Constant load tests showed no cracking at hydrogen pressures up to 100 bar and temperatures of 25 °C and 80 °C. Carbon steels absorbed up to 0.54 ppm hydrogen—below the embrittlement threshold. Austenitic stainless steels absorbed more hydrogen but were more resistant. In H_2S-saturated solutions, hydrogen uptake increased tenfold, leading to fractures in high-strength carbon steels, Super 13Cr, and Duplex 2205 [60].

This study [61] examines hydrogen transport and embrittlement resistance in dual-phase (DP) ferritic–martensitic low alloy steels (LASs). Ferritic–pearlitic and fully martensitic steels were used for comparison. Tempering reduced hardness and promoted carbide formation, increasing hydrogen diffusivity and reducing trapping—mainly due to dislocation annihilation. A higher martensite fraction lowered diffusion in both as-quenched and tempered states. Steels with ~50% tempered martensite showed the best HE resistance, highlighting design strategies for hydrogen-related applications.

When steels, especially chromium steels (e.g., 9–12% Cr), are exposed to temperatures in the range of approximately 500–650 °C for a long time, carbides of the $M_{23}C_6$ type (where M is mainly Cr, Mo, Fe) precipitate mainly at grain boundaries. This phenomenon is called sensitization and leads to the formation of zones of reduced chromium content along grain boundaries, which reduces corrosion resistance and promotes intergranular corrosion. In addition, coagulation and carbide growth reduce the impact strength and promote brittle fracture over time [68].

The authors of [69] describe the kinetics of precipitation and dissolution of $M_{23}C_6$ carbides in low-alloy steel used in the energy sector. It has been shown [70] that short-term holding at 790 °C promotes precipitation of carbides at grain boundaries, which affects the mechanical properties of steel. It has been noted [71] that an increase in the amount of $M_{23}C_6$ carbides at grain boundaries reduces the impact strength of steel during aging. The correlation between the nature of grain boundaries and carbide precipitation, as well as their effect on mechanical properties, was studied [72].

Grain boundary engineering (GBE) was applied to the GH3535 alloy (Ni-16Mo-7Cr-4Fe), which contains chains of primary molybdenum carbides that complicate uniform grain refinement. This study examined how primary carbide distribution affects grain boundary network (GBN) evolution. Cross-rolling produced finer, more dispersed carbides, promoting multiple twinning and a higher fraction of Σ3n grain boundaries. In contrast, aligned carbide strings led to particle-stimulated nucleation (PSN) and increased general high-angle boundaries, while simultaneously hindering grain boundary migration and

limiting twin-rich grain cluster formation. As a result, Σ3n boundary enhancement was suppressed [73].

Growth and coagulation of carbides at grain boundaries reduce the impact strength and promote brittle fracture. Sensitization leads to intergranular corrosion, especially in aggressive environments.

To reduce or prevent carbide precipitation, stabilized steels (e.g., 321 or 347) with Ti or Nb, a lower carbon content (e.g., 304L), and heat treatment (solution annealing) can be used [74].

When steel cools after melting, heat treatment, or elevated temperatures, sulfur and manganese tend to diffuse to the grain boundaries, where they form MnS inclusions. These inclusions can affect the mechanical properties of steel, in particular, its corrosion resistance and ductility [75–79].

The authors of [75] describe the various stages of MnS precipitation in high-carbon steel, including formation at grain boundaries and interaction with oxide inclusions. Article [76] analyzes the formation of MnS inclusions during heat treatment and their impact on the mechanical properties of steel. The authors of [77] examine the diffusion and precipitation of MnS at the interface between Mn-Al-Si oxides and steel. The authors of [78] describe the role of MnS inclusions in intergranular corrosion and depassivation of sensitized stainless steel. The authors of [78] describe the role of MnS inclusions in intergranular corrosion and depassivation of sensitized stainless steel.

The authors of [79] investigate how oxygen content influences MnS formation during cooling and heat treatment. Increased oxygen promotes the transformation of MnS morphology from Type II to Type I by facilitating oxide formation during early solidification, shifting the reaction from eutectic to monotectic. Higher oxygen levels reduce nucleation energy, enhancing heterogeneous nucleation. During slow cooling and heat treatment, the elevated oxygen content accelerates sulfide coarsening and significantly increases inclusion size, consistent with Ostwald ripening theory.

Reducing the sulfur and manganese content, as well as controlling thermal conditions, can help minimize the formation of harmful MnS inclusions [80]. For example, [81] studied the effect of tellurium (Te) treatment on the morphology of manganese sulfide (MnS) inclusions in steels with a high and low sulfur content. This study showed that the addition of tellurium changes the size and shape of MnS inclusions, promoting the formation of spherical or wrapped inclusions, which improves the machinability and mechanical properties of steel. The optimum Te/S ratio is approximately 0.5.

An increase in sulfur content leads to an increase in the number of filamentous MnS inclusions, which negatively affects the properties of steel. At a low sulfur content, most MnS inclusions are spherical or spindle-shaped, which is less harmful to mechanical properties [82].

The following technological operations can be used to restore the surface of the rotor shaft:
Surfacing (restorative build-up):
Performed using arc welding with preheat temperature of 250–300 °C;
Interpass temperature controlled within <350 °C;
Final layer grinding followed by honing to achieve Rz < 5.0 μm on reconditioned surfaces.
Post-weld Heat Treatment (PWHT):
Carried out at 620 ± 10 °C for 8 h, followed by controlled cooling in furnace atmosphere;
Aimed at reducing residual stresses and restoring toughness in 38KhN3MFA material.
Machining operations:
Honing and finishing using LCLs based on sunflower oil;
Feed rate: 0.05–0.1 mm/rev, cutting speed: 60–90 m/min, depth of cut: 0.2–0.3 mm;
LCL application pressure: 0.2 MPa, temperature: 25 ± 2 °C.

The repaired rotor sections were subjected to mechanical validation procedures, including Brinell hardness measurements (achieving 275–280 HB), ultrasonic non-destructive testing, and surface roughness control (Rz < 5.0 μm). The absence of defects and stable post-repair performance during more than 25,000 h of operation confirmed the effectiveness of the applied repair technologies.

4.2. The Main Reasons for the Movement of Carbides to the Grain Boundaries

4.2.1. Increased Diffusion Along Grain Boundaries

Grain boundaries are zones with high energy, which promotes faster diffusion of atoms, especially when exposed to high temperatures for a long time. This leads to the re-deposition of carbides, such as $M_{23}C_6$, at grain boundaries [83–87].

4.2.2. Dissolution of Intra-Grain Carbides

During prolonged thermal exposure, small carbides inside the grains can dissolve, and carbon and alloying element atoms migrate to the grain boundaries, where new, larger carbides are formed [85,88–91].

4.2.3. Redeposition of Carbides at Grain Boundaries

Grain boundaries serve as favorable places for carbide nucleation due to the presence of crystal lattice defects, which reduces the energy barrier for the formation of new phases [92–97].

4.2.4. Growth and Coagulation of Carbides

Over time, carbides at grain boundaries can grow and combine to form larger particles, which changes the mechanical properties of steel; in particular, it reduces its ductility and impact strength [93,98–104].

4.2.5. The Effect of Thermal Aging

Prolonged thermal aging promotes the formation of carbides at grain boundaries, which can lead to a decrease in corrosion resistance and mechanical properties of the material [99–103,105–110].

4.3. Influence of Alloying Elements and Microstructure Parameters on Diffusion and Hydrogen Embrittlement

Attention should also be paid to the effect of alloying elements and microstructure parameters on the properties of steels after their hydrogen saturation [111–118].

The effect of alloying elements on hydrogen brittleness and diffusion is studied in [111–114].

The authors of [111] investigated the effect of alloying elements (Cr, Mo, Mn, Ni) on hydrogen diffusion and embrittlement in martensitic steels. It was found that Cr and Mo reduce the hydrogen diffusion coefficient but can increase the tendency to brittleness due to the accumulation of hydrogen at grain boundaries. A comparison was made [112] of the effect of hydrogen saturation on the mechanical properties of various alloys, including the austenitic stainless steel AISI 321. It was found that some alloys demonstrate high resistance to hydrogen embrittlement. The authors of [113] analyzed the effect of microstructure and alloying on the resistance of steels to hydrogen embrittlement. In particular, the role of bainite structure and chromium content is studied. The authors of [114] investigated the effect of Ni, Cr, and Mo on hydrogen diffusion and embrittlement in martensitic steels. It was shown that these elements can reduce the hydrogen diffusion coefficient but at the same time increase the hydrogen concentration on the surface, which contributes to brittleness.

The authors of [115] investigated the effect of nanoscale NbC precipitates (~10 nm) on the hydrogen embrittlement of martensitic steel. It was found that NbC plays a dual role: on the one hand, it acts as a trap for hydrogen, reducing its accumulation in critical zones, and on the other hand, it can negatively affect the texture and resistance to crack propagation. The authors of [116] found that nanoscale NbC particles effectively trap hydrogen, reducing its diffusion and increasing resistance to hydrogen embrittlement in steels. In [117], it was found that hydrogen reduces the binding energy at the boundaries, which contributes to intergranular fracture. Crack formation along strain twins in TWIP steels is also observed. The authors of [118] investigated the effect of hydrogen saturation on the mechanical properties of medium manganese steels. In particular, they analyzed how the microstructure and manganese content affect the tendency to hydrogen embrittlement. The results show that optimizing the microstructure can improve the resistance to hydrogen exposure, reducing the risk of brittle fracture. The authors of [119] found that the main factor affecting the susceptibility to hydrogen embrittlement is the strength of the steel. Among the studied microstructures, fine-grained pearlite has the lowest tendency to hydrogen embrittlement, followed by bainite, and tempered martensite shows the highest sensitivity.

4.4. Application of Screening Analyses and Computer Vision Methods

The prevention of catastrophic destruction of components and structural parts can be achieved through the use of screening analyses, which include the analysis of separated fragments of particles and chips formed during repair work, as well as the analysis of wear particles in the case of tribomechanical components [25,120–142].

To identify detached particles, computer vision methods can be used, for which we already have some developments [143–157].

Also, studies of such scientific and technical problems related to the impact of technological environments, hydrogen, material destruction, and other factors are considered in a different context in the following publications [158–194].

This table (Table 3) is based on our experimental results and the previous literature. It provides a structured view of the advantages and limitations of each method in the context of rotor degradation monitoring.

Table 3. Comparative effectiveness of diagnostic methods used for hydrogen charging assessment in 38KhN3MFA rotor shafts.

Method	Sensitivity to Early Damage	Hydrogen Detection	Spatial Resolution	Application	Remarks
Metallography (SEM/OM)	High	Indirect	~1 μm	Laboratory	Reveals microcracks, carbide redistribution, inclusions
Fractography of chips	Medium	Indirect	~1 μm	Field and lab	Useful for real-time wear/degradation trends
Hydrogen content in chips	High	Direct (ppm-level)	Local bulk	Lab	Requires sample prep; correlates with structural degradation
Electrochemical testing	Medium	Indirect	Macro (~mm)	Lab	Good for coolant evaluation and general corrosion resistance
Magnetic/eddy current tests	Medium	No	~0.1–1 mm	Field	Detects discontinuities; limited for internal damage
Computer vision (chip wear)	Medium–High	No	Image resolution-based	Field and lab	Promising for automation and continuous monitoring

It should also be noted that the elastic deformations of the rotor and its supporting structures significantly affect the dynamic loads acting on the rotor shaft and, consequently, the degradation processes. This issue is discussed, in particular, in publication [195].

Considering that the bearings mounted on the rotor shaft play a crucial role in ensuring the reliable operation of power equipment [135,195], this must be taken into account in

future design decisions, especially in light of the complex changes occurring during long-term operation.

Similar approaches to force distribution and control are used in other dynamic systems, such as vehicle dynamics during curve following, where optimal longitudinal motion relies on precise traction/braking balance [196].

5. Conclusions

Hydrogen saturation of steel during long-term operation can significantly change the properties of the metal matrix, carbides, sulphides, and intermetallic content, mainly through hydrogen embrittlement mechanisms, changes in electronic properties, and the formation of localized defects. These changes can have a significant impact on the overall mechanical properties of steel, including its hardness, strength, and ductility, which affects machining.

This paper presents a scheme of redistribution of carbides in structural components in the initial state and after long-term operation. For these states, the schemes of rotor shaft turning are visualized, taking in to account some features of the microstructure. It is noted that during long-term operation, a number of alloy properties are affected by changes in the parameters of structural components caused by the action of hydrogen-containing media under these conditions.

It was found that material samples cut from differently degraded areas of power equipment and with different operating times are characterized by a corrosion resistance that is 8. . .17% lower than that of steels in their original state.

During machining (repair technologies), an increase in the hydrogen content in the chips was recorded: both in those formed directly during machining and in those released from the degraded areas of the rotor shaft. In areas on the border between intact and degraded zones, the hydrogen concentration was 6.84–7.12 ppm, and in the most damaged areas it was 7.12–7.94 ppm. The surface quality of the steel samples when honed using LCL_s improved by almost 1.5 times compared to LCL_p, which indicates the prospects of using vegetable oil as an LCL. In the undegraded areas of the rotor shaft, the recorded hydrogen concentration ranged from 2.1 to 4.4 ppm. In addition, it was found that the increase in the maximum hydrogen concentration in the chips coincides with an increase in surface roughness. This may indicate the existence of a range within which the interaction of hydrogen with LCL and the gradual moistening of the structural components of steel provides optimal roughness values during machining of the turbogenerator rotor shaft. The increase in the degree of dispersion, in particular due to degradation processes in the studied areas, caused an increase in the hydrogen concentration. This, in turn, led to a change in the intensity and nature of material destruction during machining.

Based on the results of the experimental data, regression equations and approximation reliability R^2 values were obtained to describe the change in the electrochemical parameters of 38KhN3MoA steel samples after 200, 225, 250, and up to 350 thousand hours of operation.

Hydrogen has a significant effect on the mechanical properties of steels, contributing to hydrogen embrittlement, especially under prolonged thermal loading.

It was found that the hydrogen embrittlement (HEB) in steels such as CLAM changes with the increase in the aging duration, in particular due to the precipitation of carbides ($M_{23}C_6$, MX), the formation of Laves phases, and orientational bonds with the matrix.

Thermal aging at 550–650 °C leads to sensitization and localized depletion of chromium at grain boundaries, which reduces corrosion resistance and promotes intergranular corrosion.

Some alloying elements (Cr, Mo, Ni) reduce the diffusion of hydrogen, but can disrupt its localization at grain boundaries, increasing the risk of brittle fracture.

Precipitation of carbides and MnS inclusions at grain boundaries significantly changes the impact strength and corrosion resistance of steels.

Precipitation of $M_{23}C_6$ carbides and their coagulation leads to a decrease in ductility and promotes brittle fracture.

MnS inclusions, in particular those formed during cooling, affect intercrystallite titanium corrosion and mechanical properties; their morphology and distribution can be controlled by controlling sulfur, manganese, and tellurium.

The use of stabilized steels (with Ti or Nb), steel with a reduced carbon content (304L), and heat treatment (solution annealing) can reduce the risk of degradation.

Identification and monitoring of wear processes using computer vision and particle analysis is an effective tool for preventing catastrophic damage.

The analysis of separated wear particles, including samples obtained during maintenance, allows you to assess the current condition of materials.

Computer vision and neural network methods are actively used to classify wear particles, which opens up prospects for automated condition diagnostics.

The development and implementation of screening methods (based on chip morphology, wear particles) allows for early detection of damage, which is critical for structural safety.

This study highlights the significance of hydrogen-induced microstructural changes in 38KhN3MFA steel used in turbine rotor shafts, particularly under long-term operational conditions in hydrogen-cooled environments. The presence and distribution of complex carbides, intermetallic phases, and microstructural defects were shown to directly affect hydrogen accumulation and the initiation of degradation processes. Based on these findings, the following future research directions and engineering recommendations are proposed:

- Regular chip analysis should be implemented as part of turbine maintenance protocols to monitor early-stage degradation and material instability.
- Computer vision integration is recommended for the automated classification and morphometric evaluation of wear particles and cutting chips, enhancing diagnostic accuracy and consistency.
- Machine learning algorithms should be developed and trained for intelligent classification of wear debris, utilizing shape, texture, and fractographic features as input parameters for failure prediction models.
- In situ hydrogen detection techniques, including sensor-based or spectroscopic methods, should be investigated to enable real-time tracking of hydrogen transport and accumulation in rotor steel microstructures.
- Comparative studies on alternative steel grades, such as Cr-Mo or Ni-based alloys, are needed to identify materials with superior resistance to hydrogen embrittlement under similar thermal and operational loads.
- Microstructural evolution studies should focus on the role of secondary phases (e.g., σ-phase, Laves phase, intermetallics like Ni_3Mo, Fe_2Mo) in promoting localized embrittlement, especially at grain boundaries and carbide–matrix interfaces.
- Finite element simulations and microstructure-based modeling can support the prediction of stress concentration zones, trap saturation effects, and critical hydrogen levels leading to mechanical failure.

These research directions will contribute to the development of advanced diagnostic tools and more hydrogen-resistant materials for critical rotating equipment in the energy sector.

Author Contributions: Conceptualization, A.I.B. and V.O.K.; Methodology, A.I.B., V.O.K., M.R.H., V.O.B., I.V.R., M.A.K. and T.K.P.; Software, V.O.K., M.R.H., V.O.B., I.V.R., M.A.K. and T.K.P.; Formal

analysis, A.I.B., V.O.B. and I.V.R.; Investigation, V.O.K., M.R.H., V.O.B. and I.V.R.; Resources, V.O.K., M.R.H., V.O.B., I.V.R., M.A.K. and T.K.P.; Data curation, A.I.B., V.O.K., M.R.H. and V.O.B.; Writing—review & editing, A.I.B.; Visualization, V.O.K., M.R.H., V.O.B., I.V.R., M.A.K. and T.K.P.; Supervision, A.I.B.; Project administration, A.I.B.; Funding acquisition, A.I.B. All authors have read and agreed to the published version of the manuscript.

Funding: The authors acknowledge the Polish Academy of Sciences (PAN, Poland) and National Academy of Sciences of Academy of Ukraine (NANU, Ukraine) for partial support in the framework of a joint Polish-Ukrainian project entitled "Evaluation of operational changes of nanostructure and materials properties in "green" hydrogen systems" for the years 2025–2027 under the agreement on scientific cooperation between the PAN and NANU.

Data Availability Statement: The original contributions presented in this study are included in the article. Further inquiries can be directed to the corresponding author.

Conflicts of Interest: Author Igor V. Ripey was employed by the Service Companies Galremenergo, PJSC "DTEK Zakhidenergo". The remaining authors declare that the research was conducted in the absence of any commercial or financial relationships that could be construed as a potential conflict of interest.

Abbreviations

TGV	turbogenerator with hydrogen cooling
TA	Turbo aggregate (turbine + turbogenerator)
TG	hydrogen-cooling turbogenerator
ppm	parts per million
Ecor	corrosion potential
Icor	corrosion current density
LCL	lubricating cooling liquid
LCLs	lubricating cooling liquid based on sunflower oils
LCLr	lubricating cooling liquid based on rapeseed oils
LCLp	lubricating cooling liquid based on petroleum oil
pH	indicator of the acidity or alkalinity of a solution
°C	degrees Celsius—Celsius temperature
Rz	roughness values (dry cutting)
Rzp	roughness values (after LCLp cutting)
Rzs	roughness values (after LCLs cutting)
CH	hydrogen concentration

References

1. Chernousenko, O.; Rindyuk, D.; Peshko, V.; Goryazhenko, V. Development of a Technological Approach to the Control of Turbine Casings Resource for Supercritical Steam Parameters. *East. Eur. J. Enterp. Technol.* **2018**, *2*, 51–56. [CrossRef]
2. Gakal, P.; Ovsiannykova, O.; Przybysz, J.; Tretiak, O. Analysis of the temperature field of the rotor of 550-MW turbogenerator with direct hydrogen cooling. *Prz. Elektrotechniczny* **2017**, *93*, 43–47. Available online: http://pe.org.pl/articles/2017/2/11.pdf (accessed on 9 July 2025).
3. Chernousenko, O.; Peshko, V.; Nikulenkova, T.; Rindyuk, D. Extension of the operating time of high-speed turbines of nuclear power plants. In Proceedings of the 2020 IEEE 7th International Conference on Energy Smart Systems (ESS), Kyiv, Ukraine, 2–4 November 2020; pp. 101–104. [CrossRef]
4. Tretiak, O.; Kritskiy, D.; Kobzar, I.; Sokolova, V.; Arefieva, M.; Tretiak, I.; Denys, H.; Nazarenko, V. Modeling of the stress–strain of the suspensions of the stators of high-power turbogenerators. *Computation* **2022**, *10*, 191. [CrossRef]
5. Kadhem, B.T.; Shuhati, H.W.; Alhasnawi, B.N.; Bureš, V. Account of Additional Factors for Damping Torsional Oscillations. *Heliyon* **2024**, *10*, e23995. [CrossRef] [PubMed]
6. Manikandan, P.; Khan, F.A. Analysis of Multimode Oscillations Caused by Subsynchronous Resonance on Generator Shaft. *Eur. J. Electr. Eng.* **2018**, *20*, 455–468. [CrossRef]
7. Dowson, D.; Bauer, D. Remaining Life Assessment of Steam Turbine and Hot Gas Expander Components. In Proceedings of the Asia Turbomachinery & Pump Symposium, Singapore, 22–25 February 2016. [CrossRef]

8. Barella, S.; Bellogini, M.; Boniardi, M.; Cincera, S. Failure analysis of a steam turbine rotor. *Eng. Fail. Anal.* **2011**, *18*, 511–519. [CrossRef]
9. Glotka, O.A. Distribution of Alloying Elements in Carbides of Refractory Nickel Alloys under the Conditions of Equiaxial Crystallization. *Mater. Sci.* **2021**, *56*, 714–721. [CrossRef]
10. Ol'shanetskii, V.E.; Glotka, A.A.; Klochikhin, V.V. Prediction of carbide liquidus and carbide composition of the Ni-14Cr-9Co-5Ti-3AI-3Ta-3.5W-1.5Mo-0.15Hf-0.1C system. *Functional Mater.* **2021**, *28*, 359–365. [CrossRef]
11. Glotka, A.A.; Moroz, A.N. Comparison of the effects of carbides and nonmetallic inclusions on formation of fatigue microcracks in steels. *Metal Sci. Heat Treat.* **2019**, *61*, 521–524. [CrossRef]
12. Dmytrakh, I.M.; Leshchak, R.L.; Syrotyuk, A.M.; Barna, R.A. Effect of Hydrogen Concentration on Fatigue Crack Growth Behaviour in Pipeline Steel. *Int. J. Hydrogen Energy* **2017**, *42*, 6401–6408. [CrossRef]
13. Dmytrakh, I.M.; Leshchak, R.L.; Syrotyuk, A.M. Effect of Hydrogen Concentration on Strain Behaviour of Pipeline Steel. *Int. J. Hydrogen Energy* **2015**, *40*, 4011–4018. [CrossRef]
14. Ostash, O.P.; Vytvytskyi, V.I. Duality of the Action of Hydrogen on the Mechanical Behavior of Steels and Structural Optimization of Their Hydrogen Resistance. *Mater. Sci.* **2012**, *47*, 421–437. [CrossRef]
15. Mohtadi-Bonab, M.A.; Szpunar, J.A.; Basu, R.; Eskandari, M. The Mechanism of Failure by Hydrogen Induced Cracking in an Acidic Environment for API 5L X70 Pipeline Steel. *Int. J. Hydrogen Energy* **2015**, *40*, 1096–1107. [CrossRef]
16. Fan, Y.; Ma, C.; Li, S.; Ding, W.; Zhang, H. A Review on the Effect of Microstructure on Hydrogen Induced Cracking Behaviour in Pipeline and Pressure Vessel Steels. *J. Phys. Conf. Ser.* **2020**, *1635*, 012055. [CrossRef]
17. Barrera, O.; Bombac, D.; Chen, Y.; Daff, T.D.; Galindo-Nava, E.; Gong, P.; Haley, D.; Horton, R.; Katzarov, I.; Kermode, J.R.; et al. Understanding and Mitigating Hydrogen Embrittlement of Steels: A Review of Experimental, Modelling and Design Progress from Atomistic to Continuum. *J. Mater. Sci.* **2018**, *53*, 6251–6290. [CrossRef] [PubMed]
18. Martin, M.L.; Connolly, M.J.; DelRio, F.W.; Slifka, A.J. Hydrogen Embrittlement in Ferritic Steels. *Appl. Phys. Rev.* **2020**, *7*, 041302. [CrossRef] [PubMed]
19. Khatib Zadeh Davani, R.; Mohtadi-Bonab, M.A.; Yadav, S.; Entezari, E.; Cabezas, J.F.A.; Szpunar, J. Effect of Quench Tempering on Hydrogen Embrittlement and Corrosion Behavior of X100 Pipeline Steel. *Metals* **2023**, *13*, 841. [CrossRef]
20. International Atomic Energy Agency (IAEA). *Mitigation of Hydrogen Hazards in Severe Accidents in Nuclear Power Plants*; IAEA-TECDOC-1661; IAEA: Vienna, Austria, 2011; ISBN 978-92-0-116510-7. Available online: https://www-pub.iaea.org/mtcd/publications/pdf/te_1661_web.pdf (accessed on 5 May 2025).
21. Park, B.; Kim, Y.; Hwang, I.-J. Risk Assessment of Explosion Accidents in Hydrogen Fuel-Cell Rooms Using Experimental Investigations and Computational Fluid Dynamics Simulations. *Fire* **2023**, *6*, 390. [CrossRef]
22. International Atomic Energy Agency (IAEA). *Hydrogen Phenomena During Severe Accidents in Water Cooled Reactors*; IAEA-TCS-72; IAEA: Vienna, Austria, 2021; p. 90, ISSN 1018-551. Available online: https://www-pub.iaea.org/MTCD/publications/PDF/TCS-72web.pdf (accessed on 9 July 2025).
23. Multinational Design Evaluation Programmer (MDEP). *Design-Specific Technical Report TR-HPR1000WG-01: Hydrogen Control During Severe Accidents*; OECD Nuclear Energy Agency: Paris, France, 2020. Available online: https://www.oecd-nea.org/mdep/documents/TR-HPR1000WG-01%20Hydrogen%20Control%20During%20Severe%20Accidents_clean%20copy_FINAL.pdf (accessed on 9 July 2025).
24. Liu, F.; Sun, Z.; Ding, M.; Bian, H. Research Progress of Hydrogen Behaviors in Nuclear Power Plant Containment under Severe Accident Conditions. *Int. J. Hydrogen Energy* **2021**, *46*, 36477–36502. [CrossRef]
25. Balitskii, A.I.; Syrotyuk, A.M.; Havrilyuk, M.R.; Balitska, V.O.; Kolesnikov, V.O.; Ivaskevych, L.M. Hydrogen Cooling of Turbo Aggregates and the Problem of Rotor Shafts Materials Degradation Evaluation. *Energies* **2023**, *16*, 7851. [CrossRef]
26. Balitskii, A.I.; Havrilyuk, M.R.; Balitska, V.O.; Kolesnikov, V.O.; Ivaskevych, L.M. Increasing turbine hall safety by using fire-resistant, hydrogen-containing lubricant cooling liquid for rotor steel mechanical treatment. *Energies* **2023**, *16*, 535. [CrossRef]
27. Jaworski, J.; Trzepiecínski, T. Research on durability of turning tools made of low-alloy high-speed steels. *Kov. Mater. Met. Mater.* **2016**, *54*, 17–25. [CrossRef]
28. Jaworski, J.; Trzepieciński, T. Surface Layer Properties of Low-Alloy High-Speed Steel after Grinding. *Acta Mech. Autom.* **2016**, *10*, 275–279. [CrossRef]
29. Jaworski, J.; Trzepiecinski, T. Quality assurance of machine repair in production plants. *Acta Metall. Slovaca* **2017**, *23*, 387–393. [CrossRef]
30. Korniy, S.A.; Zin, I.M.; Danyliak, M.-O.M.; Rizun, Y.Y. Eco-Friendly Metal Corrosion Inhibitors Based on Natural Polymers (A Review). *Mater. Sci.* **2023**, *58*, 567–578. [CrossRef]
31. Korniy, S.A.; Zin, I.M.; Tymus, M.B.; Khlopyk, O.P.; Holovchuk, M.Y. Steel Corrosion Inhibition by Microbial Polysaccharide and Tartrate Mixture. *J. Bio- Tribo-Corros.* **2022**, *8*, 6. [CrossRef]
32. Balyts'kyi, O.I.; Kolesnikov, V.O.; Havrylyuk, M.R. Influence of lubricating liquid on the formation of the products of cutting of 38KhN3MFA steel. *Mater. Sci.* **2019**, *54*, 722–727. [CrossRef]

33. Balyts'kyi, O.I.; Kolesnikov, V.O.; Havrylyuk, M.R. Influence of modification of 38KhN3MFA steel on the structural-phase state and cutting products under variable technological conditions. *Mater. Sci.* **2020**, *55*, 915–920. [CrossRef]
34. Balitskii, O.A.; Kolesnikov, V.O.; Balitskii, A.I.; Havrylyuk, M.R.; Eliasz, J. Hydrogen effect on the high-nickel surface steel properties during machining and wear with lubricants. *Arch. Mater. Sci. Eng.* **2020**, *104*, 49–57. [CrossRef]
35. Atrens, A.; Liu, Q.; Tapia-Bastidas, C.; Gray, E.; Irwanto, B.; Venezuela, J.; Liu, Q. Influence of Hydrogen on Steel Components for Clean Energy. *Corros. Mater. Degrad.* **2020**, *1*, 3–26. [CrossRef]
36. Smiyan, O.D. *Hydrogen and Metal Fracture of Long-Term Operating Structures*; Panasyuk, V.V., Ed.; E.O. Paton Electric Welding Institute of NAS of Ukraine, Naukova Dumka: Kyiv, Ukraine, 2018; 344p.
37. Panait, C.; Bendick, W.; Fuchsmann, A.; Gourgues-Lorenzon, A.-F.; Besson, J. Study of the Microstructure of the Grade 91 Steel after More than 100,000 h of Creep Exposure at 600 °C. Preprint 2010. Available online: https://minesparis-psl.hal.science/hal-00509625/document (accessed on 6 May 2025).
38. Dmytrakh, I.M.; Syrotyuk, A.M.; Leshchak, R.L. *Fracture and Strength of Tubular Steels in Hydrogen-Containing Environments*; Prostir-M: Lviv, Ukraine, 2020; 222p.
39. Ostash, O.P.; Vol'demarov, O.V.; Hladysh, P.V. Cyclic crack Resistance of the Steels of Bends of Steam Pipelines After Long-Term Operation. *Mater. Sci.* **2013**, *48*, 427–437. [CrossRef]
40. Ostash, O.P.; Vol'demarov, O.V.; Hladysh, P.V.; Ivasyshyn, A.D. Evaluation of the degradation of steels of steam pipelines according to their structural, mechanical, and electrochemical characteristics. *Mater. Sci.* **2011**, *46*, 431–439. [CrossRef]
41. Anmark, N.; Karasev, A.; Jönsson, P.G. The Effect of Different Non-Metallic Inclusions on the Machinability of Steels. *Materials* **2015**, *8*, 751–783. [CrossRef]
42. Hashimura, M.; Miyanishi, K.; Mizuno, A. Development of Low-Carbon Lead-Free Free-Cutting Steel Friendly to Environment. Nippon Steel Technical Report No. 96; 2007; pp. 45–49. Available online: https://www.nipponsteel.com/en/tech/report/nsc/pdf/n9608.pdf (accessed on 9 July 2025).
43. Seo, D.; Toda, H.; Kobayashi, M.; Uesugi, K.; Takeuchi, A.; Suzuki, Y. In Situ Observation of Void Nucleation and Growth in a Steel Using X-ray Tomography. *ISIJ Int.* **2015**, *55*, 1474–1482. [CrossRef]
44. Shinozuka, J.; Yachi, H.; Higashi, T.; Sando, M.; Maetani, T.; Unami, S.; Ozaki, Y. Effect of MnS on the Cutting Mechanism of Powder Metallurgy Steel in Cutting Speeds Ranging from 1 m/s to 150 m/s. *Adv. Mater. Res.* **2012**, *565*, 370–375. [CrossRef]
45. Bruce, T.; Long, H.; Slatter, T.; Dwyer-Joyce, R.S. Formation of White Etching Cracks at Manganese Sulfide (MnS) Inclusions in Bearing Steel Due to Hammering Impact Loading. *Wind Energy* **2016**, *19*, 1903–1915. [CrossRef]
46. Liu, S.; Yang, Z.; Wang, F. Behavior of MnS Inclusions during Homogenization Process in Low-Alloyed Steel FAS3420H. *High Temp. Mater. Process* **2021**, *40*, 66–76. [CrossRef]
47. Xing, L.; Fan, X.; Wang, M.; Zhao, L.; Bao, Y. The Formation Mechanism of Proeutectoid Ferrite on Medium-Carbon Sulfur-Containing Bloom. *Metall. Mater. Trans. B* **2021**, *52*, 3208–3219. [CrossRef]
48. Zhao, Y.; Li, T.; Tang, G.; Guo, H.; Yan, J.; Guo, X.; Zhu, Y. Characterization of the Morphological Evolution of MnS Inclusions in Free-Cutting Steel during Heating. *J. Mater. Res. Technol.* **2022**, *17*, 1427–1437. [CrossRef]
49. Babei, Y.I. Mechanical Treatment as a Method of Increasing the Life of Construction Alloys in Active Media. *Sov. Mater. Sci.* **1975**, *11*, 129–138. [CrossRef]
50. Nykyforchyn, H.M.; Lunarska, E.; Kyryliv, V.I.; Maksymiv, O.V. Hydrogen permeability of the surface nanocrystalline structures of carbon steel. *Mater. Sci.* **2014**, *50*, 67–73. [CrossRef]
51. Nykyforchyn, H.; Lunarska, E.; Kyryliv, V.; Maksymiv, O. Influence of hydrogen on the mechanical properties of steels with the surface nanostructure. In *Nanoplasmonics, Nano-Optics, Nanocomposites, and Surface Studies*; Shpak, A.P., Ed.; Springer Proceedings in Physics; Springer: Cham, Switzerland, 2015; Volume 167, pp. 457–465.
52. Balitskii, A.I.; Vytvytskyi, V.I.; Ivaskevich, L.M. The low-cycle fatigue of corrosion-resistant steels in high pressure hydrogen. *Procedia Eng.* **2010**, *2*, 2367–2371. [CrossRef]
53. Tkachov, V.I.; Ivas'kevych, L.M.; Mochul's'kyi, V.M. Temperature dependences of the mechanical properties of austenitic and martensitic steels in hydrogen. *Mater. Sci.* **2007**, *43*, 654–666. [CrossRef]
54. Tkachov, V.I.; Ivas'kevych, L.M.; Vytvyts'kyi, V.I. Methodological aspects of determination of hydrogen resistance of steels. Methodological aspects of determination of hydrogen resistance of steels. *Mater. Sci.* **2002**, *38*, 484–493. [CrossRef]
55. Maksimovich, G.G.; Tretyak, I.Y.; Ivas'kevich, L.M.; Slipchenko, T.V. Role of the martensite transformation in hydrogen embrittlement of unstable austenitic steels. *Soviet Mater. Sci.* **1986**, *21*, 320–323. [CrossRef]
56. Tkachov, V.I.; Levina, I.M.; Ivas'kevych, L.M. Distinctive features of hydrogen degradation of heat-resistance alloys based on nickel. *Mater. Sci.* **1997**, *33*, 524–531. [CrossRef]
57. Gu, Y.; Zhao, H.; Li, X.; Yan, W.; Xiong, L.; Chen, W.; Chen, D. Evolution of microstructure and changes in hydrogen embrittlement resistance of CLAM steel after long-term aging. *Corros. Sci.* **2024**, *232*, 112029. [CrossRef]
58. Tang, L.; Liu, W.; Gao, B.-C.; Sha, J.-T.; Bai, R.-X.; Che, B.-H.; Xu, K.; Qiao, G.-Y.; Xiao, F.-R. Study on Hydrogen Embrittlement Behavior in Heat-Affected Zone of X80 Welded Pipe. *Metals* **2025**, *15*, 414. [CrossRef]

59. Hai, C.; Zhu, Y.; Fan, E.; Du, C.; Cheng, X.; Li, X. Effects of the microstructure and reversed austenite on the hydrogen embrittlement susceptibility of Ni-Cr-Mo-V/Nb high-strength steel. *Corros. Sci.* **2023**, *218*, 111164. [CrossRef]
60. Trautmann, A.; Mori, G.; Loder, B. Hydrogen Embrittlement of Steels in High Pressure H_2 Gas and Acidified H_2S-Saturated Aqueous Brine Solution. *Berg. Hüttenmänn. Monatshefte* **2021**, *166*, 450–457. [CrossRef]
61. Rodoni, E.; Verbeken, K.; Depover, T.; Iannuzzi, M. Effect of Microstructure on the Hydrogen Embrittlement, Diffusion, and Uptake of Dual-Phase Low Alloy Steels with Varying Ferrite–Martensite Ratios. *Int. J. Hydrogen Energy* **2024**, *50 Pt A*, 53–65. [CrossRef]
62. Balitska, V.; Filipecki, J.; Ingram, A.; Shpotyuk, O. Defect characterization methodology in sintered functional spinels with PALS technique. *Phys. Status Solidi (C)* **2007**, *4*, 1317–1320. [CrossRef]
63. Balitska, V.; Shpotyuk, Y.; Filipecki, J.; Shpotyuk, O.; Iovu, M. Post-irradiation relaxation in vitreous arsenic/antimony trisulphides. *J. Non-Cryst. Solids* **2011**, *357*, 487–489. [CrossRef]
64. Balitskii, O.I.; Kvasnytska, Y.H.; Ivaskevych, L.M.; Mialnitsa, H.P.; Kvasnytska, K.H. Fatigue fracture of the blades of gas-turbine engines made of a new refractory nickel alloy. *Mater. Sci.* **2022**, *57*, 475–483. [CrossRef]
65. Balitskii, A.I.; Kvasnytska, Y.H.; Ivaskevych, L.M.; Kvasnytska, K.H.; Balitskii, O.A.; Shalevska, I.A.; Shynskii, O.Y.; Jaworski, J.M.; Dowejko, J.M. Hydrogen and Corrosion Resistance of Nickel Superalloys for Gas Turbines, Engines Cooled Blades. *Energies* **2023**, *16*, 1154. [CrossRef]
66. Kvasnytska, Y.H.; Ivaskevich, L.M.; Balitskii, A.I.; Kvasnytska, K.H.; Mialnitsa, H.P. Structural and mechanical properties of the nickel alloy of gas-turbine engine blades. *Mater. Sci.* **2022**, *57*, 688–694. [CrossRef]
67. Kawiak, M.; Balitskii, A. Embrittlement of welded joints of tram rails in city environments. *Eng. Fail. Anal.* **2018**, *85*, 97–103. [CrossRef]
68. Ivas'kevych, L.M. Influence of Alloying with Cobalt and Hafnium on the Corrosion and Hydrogen Resistances of Refractory Nickel Alloy. *Mater. Sci.* **2020**, *55*, 730–736. [CrossRef]
69. Godec, M.; Skobir Balantič, D. Coarsening Behaviour of $M_{23}C_6$ Carbides in Creep-Resistant Steel Exposed to High Temperatures. *Sci. Rep.* **2016**, *6*, 29734. [CrossRef]
70. Li, Z.; Jia, P.; Liu, Y.; Qi, H. Carbide Precipitation, Dissolution, and Coarsening in G18CrMo2–6 Steel. *Metals* **2019**, *9*, 916. [CrossRef]
71. Yu, X.F.; Zheng, D.Y.; Yang, X.F.; Wang, S.Y.; An, M.; Yan, G.B.; Xia, Y.Z.; Xing, F. Effect of Carbide Precipitation Behavior at High Temperatures on Microstructure and Mechanical Properties of M50 Steel. *J. Mater. Res. Technol.* **2022**, *18*, 1155–1165. [CrossRef]
72. Lv, X.; Chen, S.; Rong, L. Evolution of Precipitate and Its Effect on the Degradation of Impact Toughness in a Carbon- and Nitrogen-Controlled 316 Stainless Steel during Thermal Aging at 650 °C. *J. Mater. Res. Technol.* **2024**, *33*, 3728–3742. [CrossRef]
73. Han, Y.; Xue, X.; Zhang, T.; Hu, R.; Li, J. Grain Boundary Character Correlated Carbide Precipitation and Mechanical Propertiesof Ni-20Cr-18W-1Mo Superalloy. *Mater. Sci. Eng. A* **2016**, *667*, 391–401. [CrossRef]
74. Liu, T.; Yang, M.; Han, F.; Dong, J. Influence Mechanism of Silicon on Carbide Phase Precipitation of a Corrosion Resistance Nickel Based Superalloy. *Materials* **2020**, *13*, 959. [CrossRef]
75. Xia, S.; Ma, Y.; Bai, Q. Effects of the Primary Carbide Distribution on the Evolution of the Grain Boundary Character Distribution in a Nickel-Based Alloy. *Metals* **2024**, *14*, 960. [CrossRef]
76. Specialty Steel Industry of North America. Intergranular Corrosion. Available online: https://www.ssina.com/education/corrosion/intergranular-corrosion (accessed on 9 July 2025).
77. Tanaka, Y.; Pahlevani, F.; Moon, S.C.; Sahajwalla, V. In situ Characterisation of MnS Precipitation in High Carbon Steel. *Sci. Rep.* **2019**, *9*, 10096. [CrossRef] [PubMed]
78. Duan, Z.; Man, C.; Cui, H.; Cui, Z.; Wang, X. Formation Mechanism of MnS Inclusion during Heat Treatments and Its Influence on the Pitting Behavior of 316L Stainless Steel Fabricated by Laser Powder Bed Fusion. *Corros. Commun.* **2022**, *7*, 12–22. [CrossRef]
79. Liu, W.; Li, M.; Yang, S.; Xu, Z.; Huang, C.; Liu, T.; Li, J. Diffusion and Precipitation of MnS at Interface between Mn–Al–Si Oxides and Steel during Solidification. *J. Mater. Res. Technol.* **2022**, *18*, 990–997. [CrossRef]
80. Sui, H.; Wang, L.; Wang, Q.; Wang, H.; Che, D.; Li, J.; Chou, K. The Formation and Growth of Sulfides in Free-Cutting Stainless Steel. *Steel Res. Int.* **2018**, *89*, 1800179. [CrossRef]
81. Zhang, H.; Feng, G.; Liu, X.; Wang, B.; Liu, X. Effect of Sulfur Content on the Composition of Inclusions and MnS Precipitation Behavior in Bearing Steel. *Metals* **2020**, *10*, 570. [CrossRef]
82. Wang, F.; Guo, H.; Liu, W.; Yang, S.; Zhang, S.; Li, J. Control of MnS Inclusions in High- and Low-Sulfur Steel by Tellurium Treatment. *Materials* **2019**, *12*, 1034. [CrossRef]
83. Yu, Q.; Yang, X.; Lai, C.; Tong, Z. Study on MnS Inclusion Aggregation along Continuous Casting Slab Thickness of Medium Carbon Structural Steel. *Metals* **2022**, *12*, 56. [CrossRef]
84. Lee, S.-H.; Na, H.-S.; Lee, K.-W.; Choe, Y.; Kang, C.Y. Microstructural Characteristics and $M_{23}C_6$ Precipitate Behavior of the Course-Grained Heat-Affected Zone of T23 Steel without Post-Weld Heat Treatment. *Metals* **2018**, *8*, 170. [CrossRef]

85. Balyts'kyi, O.I.; Ivas'kevych, L.M.; Mochul's'kyi, V.M. Mechanical properties of martensitic steels in gaseous hydrogen. *Strength Mater.* **2012**, *44*, 64–71. [CrossRef]
86. Janovec, J.; Svoboda, M.; Kroupa, A.; Šob, M. Thermal-Induced Evolution of Secondary Phases in Cr–Mo–V Low Alloy Steels. *J. Mater. Sci.* **2006**, *41*, 3425–3433. [CrossRef]
87. Kim, H.-P.; Park, Y.-M.; Jang, H.-M.; Lim, S.-Y.; Choi, M.-J.; Kim, S.-W.; Kim, D.-J.; Hwang, S.-S.; Lim, Y.-S. Early-Stage $M_{23}C_6$ Morphology at the Phase Boundary in Type 304L Austenitic Stainless Steel Containing δ Ferrite. *Metals* **2022**, *12*, 1794. [CrossRef]
88. Oanh, N.T.H.; Viet, N.H. Precipitation of $M_{23}C_6$ Secondary Carbide Particles in Fe-Cr-Mn-C Alloy during Heat Treatment Process. *Metals* **2020**, *10*, 157. [CrossRef]
89. Silva, F.J.G.; Santos, J.; Gouveia, R. Dissolution of Grain Boundary Carbides by the Effect of Solution Annealing Heat Treatment and Aging Treatment on Heat-Resistant Cast Steel HK30. *Metals* **2017**, *7*, 251. [CrossRef]
90. Zheng, L.; Ding, Z. Characterization of $M_{23}C_6$ Carbides Precipitating at Grain Boundaries in 100Mn13 Steel. *Metall. Mater. Trans. A* **2016**, *47*, 4893–4901. [CrossRef]
91. Zhang, Y.; Zhang, Z.; Wang, H.; Li, J.; Xu, X. The Effect of Precipitate Evolution on Austenite Grain Growth in Reduced Activation Ferritic/Martensitic Steel. *Materials* **2017**, *10*, 1017. [CrossRef]
92. Yang, Z.; Jin, S.; Song, L.; Zhang, W.; You, L.; Guo, L. Dissolution of $M_{23}C_6$ and New Phase Re-Precipitation in Fe Ion-Irradiated RAFM Steel. *Metals* **2018**, *8*, 349. [CrossRef]
93. Yang, Z.; Li, K.; Li, J.; Cheng, J.; Qian, C.; Cai, J.; Huo, X.; Liu, X.; Li, S.; Liu, Q.; et al. Effects of Heating Methods on Precipitation Behavior and Nucleation Activation Energy of γ′ Phase in Iron–Nickel-Based Alloy. *Metals* **2025**, *15*, 345. [CrossRef]
94. Golański, G.; Zieliński, A.; Sroka, M.; Słania, J. The Effect of Service on Microstructure and Mechanical Properties of HR3C Heat-Resistant Austenitic Stainless Steel. *Materials* **2020**, *13*, 1297. [CrossRef] [PubMed]
95. Meixner, F.; Ahmadi, M.R.; Sommitsch, C. Cavity Nucleation and Growth in Nickel-Based Alloys during Creep. *Materials* **2022**, *15*, 1495. [CrossRef]
96. Elsevier. Grain Boundary Carbide—An Overview. ScienceDirect Topics. Available online: https://www.sciencedirect.com/topics/engineering/grain-boundary-carbide (accessed on 9 July 2025).
97. Avila, D.D.S.; Offerman, S.E.; Santofimia, M.J. Modeling the Effect of Prior Austenite Grain Size on Bainite Formation Kinetics. *Acta Mater.* **2024**, *266*, 119656. [CrossRef]
98. Long, X.; Zhang, F.; Yang, Z.; Zhang, M. Study on Bainitic Transformation by Dilatometer and In Situ LSCM. *Materials* **2019**, *12*, 1534. [CrossRef]
99. Yao, X.; Huang, J.; Qiao, Y.; Sun, M.; Wang, B.; Xu, B. Precipitation Behavior of Carbides and Its Effect on the Microstructure and Mechanical Properties of 15CrNi3MoV Steel. *Metals* **2022**, *12*, 1758. [CrossRef]
100. Sroka, M.; Zieliński, A.; Golański, G.; Pawlyta, M.; Purzyńska, H.; Novy, F. Evolution of the Microstructure and Mechanical Properties of Sanicro 25 Austenitic Stainless Steel after Long-Term Ageing. *Arch. Civ. Mech. Eng.* **2023**, *23*, 149. [CrossRef]
101. Ma, Y.; Kuang, C.; Cheng, J.; Yang, C. Influence of the Evolution of 9CrMoCoB Steel Precipitates on the Microstructure and Mechanical Properties during High-Temperature Aging. *J. Mater. Eng. Perform.* **2021**, *30*, 9029–9037. [CrossRef]
102. Zhou, Y.; Aust, K.T.; Erb, U.; Palumbo, G. Effects of Grain Boundary Structure on Carbide Precipitation in 304L Stainless Steel. *Scripta Mater.* **2001**, *45*, 49–54. [CrossRef]
103. Wang, X.; Xu, L.; Jiao, L.; Mei, J.; Zhao, Y.; Qiao, L. Microstructure Evolution during Aging and Its Effect on Mechanical Properties of a Novel Nano-Carbide Dispersion Strengthened Steel. *Mater. Sci. Eng. A* **2025**, *928*, 148064. [CrossRef]
104. Liu, D.; Ding, H.; Han, D.; Cai, M. Effect of Grain Interior and Grain Boundary κ-Carbides on the Strain Hardening Behavior of Medium-Mn Lightweight Steels. *Mater. Sci. Eng. A* **2023**, *871*, 144861. [CrossRef]
105. Fang, K.; Luo, K.; Wang, L. Effect of Microstructure on Mechanical Properties of 316 LN Austenitic Stainless Steel. *Coatings* **2022**, *12*, 1461. [CrossRef]
106. Huh, C.; An, S.; Kim, M.; Kim, C. Effect of Corrosion Characteristics on Long-Term Aging of Austenitic 304 Steel. *Appl. Sci.* **2019**, *9*, 5557. [CrossRef]
107. Wang, Z.; Gao, F.; Tang, S.; Zhou, P.; Zhang, W.; Liu, Z. Effect of Twin-Related Boundaries Distribution on Carbide Precipitation and Intergranular Corrosion Behavior in Nuclear-Grade Higher Carbon Austenitic Stainless Steel. *Corros. Sci.* **2022**, *209*, 110791. [CrossRef]
108. Aditya, D.M.; Ardy, H.; Lantang, Y.S.F.; Afrianti, Y.S.; Ilmi, N.F.F.; Pasaribu, U.S. The Study of Sigma and Carbide in Cast Austenitic Stainless-Steel Grade HH after 24 Years of High-Temperature Service. *Heliyon* **2023**, *9*, e14109. [CrossRef]
109. Lin, M.; Gottstein, G.; Shvindlerman, L.S. Generalized Gibbs–Thomson Equation for Nanoparticles at Grain Boundaries. *Acta Mater.* **2017**, *129*, 361–365. [CrossRef]
110. Banis, A.; Gomez, A.; Bliznuk, V.; Dutta, A.; Sabirov, I.; Petrov, R.H. Microstructure Evolution and Mechanical Behavior of Fe–Mn–Al–C Low-Density Steel upon Aging. *arXiv* **2023**, arXiv:2305.00481. [CrossRef]
111. Zhang, B.-G.; Zhang, X.-M.; Liu, H.-T. Precipitation Behavior of B2 and κ-Carbide during Aging and Its Effect on Mechanical Properties in Al-Containing High Strength Steel. *Mater. Charact.* **2021**, *178*, 111291. [CrossRef]

112. Balyts'kyi, O.I.; Kostyuk, I.F. Strength of welded joints of Cr-Mn steels with elevated content of nitrogen in hydrogen-containing media. *Mater. Sci.* **2009**, *1*, 97–107. [CrossRef]
113. Jürgensen, J.; Frehn, A.; Ohla, K.; Stolz, S.; Pohl, M. Effect of Hydrogen Charging on the Mechanical Properties of High-Strength Copper-Base Alloys, Austenitic Stainless Steel AISI 321, Inconel 625 and Ferritic Steel 1.4511. *Metals* **2024**, *14*, 588. [CrossRef]
114. Nanninga, N.E. Effect of Microstructure and Alloying Elements on the Resistance of Fastener Grade Steels to Hydrogen Assisted Cracking. Master's Thesis, Michigan Technological University, Houghton, MI, USA, 2005. Available online: https://digitalcommons.mtu.edu/cgi/viewcontent.cgi?article=1023&context=etds (accessed on 9 July 2025).
115. Balyts'kyi, O.I.; Krokhmal'nyi, O.O. Pitting corrosion of 12Kh18AG18Sh steel in chloride solutions. *Mater. Sci.* **1999**, *35*, 389–394. [CrossRef]
116. Zhang, S.; Wan, J.; Zhao, Q.; Liu, J.; Huang, F.; Huang, Y.; Li, X. Dual Role of Nanosized NbC Precipitates in Hydrogen Embrittlement Susceptibility of Lath Martensitic Steel. *Corros. Sci.* **2020**, *164*, 108345. [CrossRef]
117. Fan, E.; Zhang, S.; Xie, D.; Zhao, Q.; Li, X.; Huang, Y. Effect of Nanosized NbC Precipitates on Hydrogen-Induced Cracking of High-Strength Low-Alloy Steel. *Int. J. Miner. Metall. Mater.* **2021**, *28*, 249–256. [CrossRef]
118. Evers, S.; Hickel, T.; Koyama, M.; Nazarov, R.; Rohwerder, M.; Neugebauer, J.; Raabe, D.; Stratmann, M. Microstructure Effects on Hydrogen Embrittlement in Austenitic Steels: A Multidisciplinary Investigation. Max Planck Institute for Iron Research. Available online: https://www.mpie.de/3173155/Hydrogen-Embrittlement (accessed on 9 July 2025).
119. Cho, L.; Kong, Y.; Speer, J.G.; Findley, K.O. Hydrogen Embrittlement of Medium Mn Steels. *Metals* **2021**, *11*, 358. [CrossRef]
120. Nanninga, N.; Grochowsi, J.; Heldt, L.; Rundman, K. Role of Microstructure, Composition and Hardness in Resisting Hydrogen Embrittlement of Fastener Grade Steels. *Corros. Sci.* **2010**, *52*, 1237–1246. [CrossRef]
121. Balyts'kyi, O.I.; Kolesnikov, V.O. Investigation of the Wear Products of Austenitic Manganese Cast Irons. *Mater. Sci.* **2004**, *40*, 78–82. [CrossRef]
122. Balyts'kyi, O.I.; Kolesnikov, V.O.; Kubicki, E. Enhancement of the Crack Resistance of Manganese Cast Irons. *Mater. Sci.* **2005**, *41*, 67–73. [CrossRef]
123. Balytskyi, O.I.; Kolesnikov, V.O.; Kaviak, P. Tribotechnical Properties of Austenitic Manganese Steels and Cast Irons under Sliding Friction Conditions. *Fiz.-Khim. Mekh. Mater.* **2005**, *41*, 55–60, ISSN 0430-6252. Available online: https://www.scopus.com/record/display.uri?eid=2-s2.0-33645644956&origin=resultslist&sort=plf-f&src=s&sid=4f73bdf9754dfdac7256947d377c3271&sot=autdocs&sdt=autdocs&sl=17&s=AU-ID%288918120300%29&relpos=5&citeCnt=0&searchTerm= (accessed on 9 July 2025).
124. Balitskii, A.; Kolesnikov, V.; Abramek, K.F.; Balitskii, O.; Eliasz, J.; Marya, H.; Ivaskevych, L.; Kolesnikova, I. Influence of Hydrogen-Containing Fuels and Environmentally Friendly Lubricating Coolant on Nitrogen Steels' Wear Resistance for Spark Ignition Engine Pistons and Rings Kit Gasket Set. *Energies* **2021**, *14*, 7583. [CrossRef]
125. Balitskii, O.A.; Kolesnikov, V.O.; Balitskii, A.I. Wear resistance of hydrogenated high nitrogen steel at dry and solid state lubricants assistant friction. *Arch. Mater. Sci. Eng.* **2019**, *2*, 57–67. [CrossRef]
126. Balyts'kyi, O.I.; Kolesnikov, V.O.; Eliasz, J. Study of the Wear Resistance of High-Nitrogen Steels under Dry Sliding Friction. *Mater. Sci.* **2013**, *48*, 642–646. [CrossRef]
127. Balitskii, A.A.; Kolesnikov, V.A.; Vus, O.B. Tribotechnical properties of nitrogen manganese steels under rolling friction at addition of (GaSe)xIn1−x powders into contact zone. *Metallofiz. I Noveishie Tekhnologii.* **2010**, *32*, 685–695. Available online: http://scholar.google.com/scholar_lookup?title=Tribotechnical+properties+of+nitrogen+manganese+steels+under+rolling+friction+at+addition+of+(GaSe)xIn1%E2%88%92x+powders+into+contact+zone&author=Balitskii,+A.A.&author=Kolesnikov,+V.A.&author=Vus,+O.B.&publication_year=2010&journal=Metallofiz.+I+Noveishie+Tekhnologii.&volume=32&pages=685%E2%80%93695 (accessed on 9 July 2025).
128. Balitskii, A.I.; Syrotyuk, A.M.; Ivaskevich, L.M.; Balitskii, O.A.; Kochmanski, P.; Kolesnikov, V.O. Hydrogen Accelerated Nanopore Nucleation, Crack Initiation and Propagation in the Ni–Co Superalloys. *Int. J. Hydrogen Energy* **2024**, *82*, 320–332. [CrossRef]
129. Balitskii, O.I.; Kolesnikov, V.O.; Ivaskevych, L.M.; Havrylyuk, M.R. The Influence of Specific Features of Load and Hydrogen Charging on Steel Tribotechnical Properties. *Mater. Sci.* **2023**, *58*, 505–512. [CrossRef]
130. Balyts'kyi, O.I.; Kolesnikov, V.O. Investigation of Wear Products of High-Nitrogen Manganese Steels. *Mater. Sci.* **2009**, *45*, 576–581. [CrossRef]
131. Skalskyi, V.; Nazarchuk, Z.Z.; Stankevych, O.; Klym, B. Influence of Occluded Hydrogen on Magnetoacoustic Emission of Low-carbon Steels. *Int. J. Hydrogen Energy* **2023**, *48*, 6146–6156. [CrossRef]
132. Balyts'kyi, O.I. Effect of Hydrogen on Structural Strength of High-nitrogen Chromium–manganese Steels. *Mater. Sci.* **2000**, *36*, 541–545. [CrossRef]
133. Balitskii, A.; Kindrachuk, M.; Volchenko, D.; Abramek, K.F.; Balitskii, O.; Skrypnyk, V.; Zhuravlev, D.; Bekish, I.; Ostashuk, M.; Kolesnikov, V. Hydrogen Containing Nanofluids in the Spark Engine's Cylinder Head Cooling System. *Energies* **2022**, *15*, 59. [CrossRef]

134. Balyts'kyi, O.I.; Kolesnikov, V.O.; Kawiak, P. Triboengineering Properties of Austenitic Manganese Steels and Cast Irons under the Conditions of Sliding Friction. *Mater. Sci.* **2005**, *41*, 624–630. [CrossRef]
135. Balitskii, A.I.; Syrotyuk, A.M.; Kolesnikov, V.O.; Balitska, V.O.; Ivaskevych, L.M.; Havrilyuk, M.R. The Effect of Absorbed Hydrogen on the Rotors of Steel Machining Products During Powerful Turbo Aggregate Repairs. *Materials* **2024**, *17*, 6257. [CrossRef]
136. Laghari, M.; Hassan, A.; Haggag, M.; Wahyudie, A.; Tayfor, M.; Elsayed, A. Comparison of Recognition Techniques to Classify Wear Particle Texture. *Eng* **2025**, *6*, 107. [CrossRef]
137. Habib, K.A.; Cano, D.L.; Heredia, J.A.; Serrano-Mira, J. Analysis of the Hardness Ratio Effect on the Tribological Performance of NiCrBSi Coating/Debris Particles Using the Stribeck Curve. *Wear* **2021**, *486–487*, 204081. [CrossRef]
138. Zeng, L.; Zhang, H.; Wang, Q.; Zhang, X. Monitoring of Non-Ferrous Wear Debris in Hydraulic Oil by Detecting the Equivalent Resistance of Inductive Sensors. *Micromachines* **2018**, *9*, 117. [CrossRef] [PubMed]
139. Goncalves, A.C.; Chavarette, F.R.; Outa, R.; Godoi, L.H.A. Assistance of Analytical Ferrography in the Interpretation of Wear Test Results Carried Out with Biolubricants. *Tribol. Int.* **2024**, *197*, 109758. [CrossRef]
140. Yang, Z.; Zhao, M.; Wang, X.; Tian, X.; Hu, K.; Li, W.; Zhang, Y. Influence of the Surface Rolling Process on the Tribological and Electrical Behavior of T2 Copper Elastic Contact Pairs. *Coatings* **2025**, *15*, 615. [CrossRef]
141. Haddad, F.; Lescalier, C.; Desaigues, J.-E.; Bomont-Arzur, A.; Bomont, O. Metallurgical Analysis of Chip Forming Process when Machining High Strength Bainitic Steels. *J. Manuf. Mater. Process.* **2019**, *3*, 10. [CrossRef]
142. Guan, R.; Cheng, Y.; Xue, J.; Zhou, S.; Zhou, X.; Zhai, W. Analysis of Chip Morphology in Heavy Milling of 508III Steel Considering Different Tool Wear Conditions. *Materials* **2024**, *17*, 3948. [CrossRef]
143. Qibiao, Y.; Zhanqiang, L.; Bing, W. Characterization of Chip Formation during Machining 1045 Steel. *Int. J. Adv. Manuf. Technol.* **2012**, *63*, 881–886. [CrossRef]
144. Balitskii, O.; Kolesnikov, V. Identification of Wear Products in the Automotive Tribotechnical System Using Computer Vision Methods, Artificial Intelligence and Big Data. In Proceedings of the 2019 XIth International Scientific and Practical Conference on Electronics and Information Technologies (ELIT), Lviv, Ukraine, 16–18 September 2019; pp. 24–27. [CrossRef]
145. Balitskii, A.I.; Kolesnikov, V.O.; Balitska, V.O.; Ivaskevych, L.M.; Dowejko, J.M.; Pilecki, B.J.; Havrilyuk, M.R. Computer-Integrated Surface Image Processing of Hydrogen-Saturated Steel Wear Products. *Appl. Sci.* **2024**, *14*, 11762. [CrossRef]
146. Raadnui, S. Wear Particle Analysis—Utilization of Quantitative Computer Image Analysis: A Review. *Tribol. Int.* **2005**, *38*, 871–878. [CrossRef]
147. Laghari, M.S. Recognition of Texture Types of Wear Particles. *Neural Comp. Appl.* **2003**, *12*, 18–25. [CrossRef]
148. Laghari, M.S.; Hassan, A.; Noman, M. Classifying Wear Particles Based on Texture Analysis. In *Congress on Smart Computing Technologies. CSCT 2022*; Bansal, J.C., Sharma, H., Chakravorty, A., Eds.; Smart Innovation, Systems and Technologies; Springer: Singapore, 2023; Volume 351, pp. 161–171. [CrossRef]
149. Roylance, B.J.; Albidewi, I.A.; Laghari, M.S.; Luxmoore, A.R.; Deravi, F. Computer Aided Vision Engineering (CAVE)—Quantification of Wear Particle Morphology. *J. Soc. Tribol. Lubr. Eng.* **1994**, *50*, 111–116. Available online: https://scholar.google.com/scholar_lookup?title=Computer+Aided+Vision+Engineering+(CAVE)%E2%80%94Quantification+of+Wear+Particle+Morphology&author=Roylance,+B.J.&author=Albidewi,+I.A.&author=Laghari,+M.S.&author=Luxmoore,+A.R.&author=Deravi,+F.&publication_year=1994&journal=J.+Soc.+Tribol.+Lubr.+Eng.&volume=50&pages=111%E2%80%93116 (accessed on 9 July 2025).
150. Wu, T.; Wu, H.; Du, Y.; Kwok, N.; Peng, Z. Imaged Wear Debris Separation for On-Line Monitoring Using Gray Level and Integrated Morphological Features. *Wear* **2014**, *316*, 19–29. [CrossRef]
151. Shah, R.; Sridharan, N.V.; Mahanta, T.K.; Muniyappa, A.; Vaithiyanathan, S.; Ramteke, S.M.; Marian, M. Ensemble Deep Learning for Wear Particle Image Analysis. *Lubricants* **2023**, *11*, 461. [CrossRef]
152. He, L.; Wei, H.; Gao, W. Research on an Intelligent Classification Algorithm of Ferrography Wear Particles Based on Integrated ResNet50 and SepViT. *Lubricants* **2023**, *11*, 530. [CrossRef]
153. He, L.; Wei, H.; Wang, Q. A New Target Detection Method of Ferrography Wear Particle Images Based on ECAM-YOLOv5-BiFPN Network. *Sensors* **2023**, *23*, 6477. [CrossRef]
154. Xiao, X.; Zhang, W.; Wang, Q.; Liu, Y.; Wang, Y. Intelligent Recognition Method for Ferrography Wear Debris Images Using Improved Mask R-CNN Methods. *Lubricants* **2025**, *13*, 208. [CrossRef]
155. Wang, S.; Wu, T.; Zheng, P.; Kwok, N. Optimized CNN Model for Identifying Similar 3D Wear Particles in Few Samples. *Wear* **2020**, *460–461*, 203477. [CrossRef]
156. Sieberg, P.M.; Kurtulan, D.; Hanke, S. Wear Mechanism Classification Using Artificial Intelligence. *Materials* **2022**, *15*, 2358. [CrossRef]
157. Herwig, N.; Peng, Z.; Borghesani, P. Bridging the Trust Gap: Evaluating Feature Relevance in Neural Network-Based Gear Wear Mechanism Analysis with Explainable AI. *Tribol. Int.* **2023**, *187*, 108670. [CrossRef]

158. Li, Q.; Zhao, T.; Zhang, L.; Sun, W.; Zhao, X. Ferrography Wear Particles Image Recognition Based on Extreme Learning Machine. *J. Electr. Comput. Eng.* **2017**, *2017*, 3451358. [CrossRef]
159. Balyts'kyi, O.O. Elastic characteristics of laminated gallium and indium chalcogenides. *Mater. Sci.* **2004**, *40*, 706–709. [CrossRef]
160. Balitskii, A.I.; Dmytryk, V.V.; Ivaskevich, L.M.; Balitskii, O.A.; Glushko, A.V.; Medovar, L.B.; Abramek, K.F.; Stovpchenko, G.P.; Eliasz, J.J.; Krolikowski, M.A. Improvement of the Mechanical Characteristics, Hydrogen Crack Resistance and Durability of Turbine Rotor Steels Welded Joints. *Energies* **2022**, *15*, 6006. [CrossRef]
161. Balyts'Kyi, O.I.; Chmiel, J.; Krause, P.; Niekrasz, J.; MacIag, M. Role of hydrogen in the cavitation fracture of 45 steel in lubricating media. *Mater. Sci.* **2009**, *45*, 651–654. [CrossRef]
162. Balitskii, A.I.; Osipowicz, T.K.; Abramek, K.F.; Balitska, V.O.; Kochmański, P.; Królikowski, M.A. Hydrogen-Containing Fuel Influence on Compression-Ignition Engine Part Wear and Emissions of Toxic Substances. *Energies* **2025**, *18*, 1722. [CrossRef]
163. Balitskii, A.; Vytvytskyii, V.; Ivaskevich, L.; Eliasz, J. The high- and low-cycle fatigue behaviour of Ni-contain steels and Ni-alloys in high pressure hydrogen. *Int. J. Fatigue* **2012**, *39*, 32–37. [CrossRef]
164. Balitskii, A.; Krohmalny, O.; Ripey, I. Hydrogen cooling of turbogenerators and the problem of rotor retaining ring materials degradation. *Int J Hydrogen Energy* **2000**, *25*, 167–171. [CrossRef]
165. Balyts'kyi, O.I.; Ripei, I.V.; Protsakh, K.A. Reliability of Steam Pipelines of Thermal Power Plants in the Course of Long-term Operation. *Mater. Sci.* **2006**, *42*, 461–465. [CrossRef]
166. Krechkovs'ka, H.V.; Student, O.Z.; Nykyforchyn, H.M. Diagnostics of the engineering state of steam pipeline of thermal power plants by the hardness and crack resistance of steel. *Mater. Sci.* **2019**, *54*, 627–637. [CrossRef]
167. Pokhmurs'kyi, V.I.; Kopylets', V.I.; Kornii, S.A. Modeling of the corrosion-electrochemical processes on the metal–electrolyte interface. *Mater. Sci.* **2013**, *49*, 59–62. [CrossRef]
168. Krechkovska, H.; Student, O.; Hredil, M.; Tsybailo, I.; Holovchuk, M.; Shtoyko, I. Visualization of fractographic signs of operational degradation of heat-resistant steel for estimating its actual structure-mechanical state. *Procedia Struct. Integr.* **2022**, *42*, 1398–1405. [CrossRef]
169. Djukic, M.B.; Bakic, G.M.; Zeravcic, V.S.; Rajicic, B.; Sedmak, A.; Mitrovic, R.; Miskovic, Z. Towards a Unified and Practical Industrial Model for Prediction of Hydrogen Embrittlement and Damagein Steels. *Procedia Struct. Integr.* **2016**, *2*, 604–611. [CrossRef]
170. Zvirko, O.; Dzioba, I.; Hredil, M.; Pała, R.; Oliynyk, O.; Furmańczyk, P. Specimen Size Effectonthe Tensile Properties of Rolled Steel of Long-Term-Operated Portal Crane. *Materials* **2023**, *16*, 3017. [CrossRef] [PubMed]
171. Tkach, P.; Reviakina, O.; Kryvosheia, A.; Ustynenko, O.; Protasov, R. Meshing characteristics of profile shifted cylindrical quasi-involute arc-tooth-trace gears. Part 1. *Theor. Base. Stroj. Casopis.* **2022**, *72*, 201–210. [CrossRef]
172. Andreikiv, O.Y.; Dolins'ka, I.Y.; Shtoiko, I.P.; Raiter, O.K.; Matviiv, Y.Y. Evaluation of the residual service life of main pipelines with regard for the action of media and degradation of materials. *Mater. Sci.* **2019**, *54*, 638–646. [CrossRef]
173. Terniuk, M.E.; Kryvosheia, A.V.; Krasnoshtan, A.M.; Tkach, P.M.; Lutskii, S.V. Gear manufacturing accuracy prediction, control, and management. In *Novikov/Conform. Gearing*; Springer: Berlin/Heidelberg, Germany, 2023; pp. 215–323. [CrossRef]
174. Onysko, O.; Kopei, V.; Vytvytskyi, V.; Vriukalo, V.; Lukan, T. Calculation of the accuracy of the drill-string nc13 thread profile turned from difficult-to-machine steel. In *Advanced Manufacturing Processes V. InterPartner 2023. Lecture Notes in Mechanical Engineering*; Springer: Cham, Switzerland, 2024; pp. 182–192. [CrossRef]
175. Yasniy, P.V.; Okipnyi, I.B.; Maruschak, P.O.; Panin, S.V.; Konovalenko, I.V. Crack tip strain localisation on mechanics of fracture of heat resistant steel after hydrogenation. *Theor. Appl. Fract. Mech.* **2013**, *63–64*, 63–68. [CrossRef]
176. Bovsunovsky, A.; Shtefan, E.; Peshko, V. Modeling of the circumferential crack growth under torsional vibrations of steam turbine shafting. *Theor. Appl. Fract. Mech.* **2023**, *2023*, 103881. [CrossRef]
177. Hembara, O.V.; Chepil, O.Y.; Hembara, N.T.; Syrotyuk, A.M. Evaluation of the Influence of the Hydrogenation of Metal on the Durability of Heat-Exchanger Tubes of Steam Generators. *Mater. Sci.* **2022**, *58*, 325–330. [CrossRef]
178. Pokhmurs'kyi, V.I.; Vasyliv, K.B. Influence of hydrogen on the friction and wear of metals (a survey). *Mater. Sci.* **2012**, *48*, 125–138. [CrossRef]
179. Chernousenko, O.; Rindyuk, D.; Peshko, V.; Bednarska, I. Effect of Start-Up Operating Modes on the Cyclic Damage of Thermal Power Plant Units. In Proceedings of the 2022 IEEE 8th International Conference on Energy Smart Systems (ESS), Kyiv, Ukraine, 7–9 September 2022; pp. 233–238. [CrossRef]
180. Khoma, M.S.; Korniy, S.A.; Vynar, V.A.; Datsko, B.M.; Maksishko, Y.; Dykha, O.V.; Bukliv, R.L. Influence of hydrogen sulfide on the carbon-dioxide corrosion and the mechanical characteristics of high-strength pipe steel. *Mater. Sci.* **2022**, *1*, 805–812. [CrossRef]
181. Czapla, K.; Żaba, K.; Kot, M.; Nejman, I.; Madej, M.; Trzepieciński, T. Tribological Performance of Anti-Wear Coatings on Tools for Forming Aluminium Alloy Sheets Used for Producing Pull-Off Caps. *Materials* **2023**, *16*, 6465. [CrossRef] [PubMed]
182. Trzepieciński, T.; Szwajka, K.; Szewczyk, M.; Barlak, M.; Zielińska-Szwajka, J. Effect of Countersample Coatings on the Friction Behaviour of DC01 Steel Sheets in Bending-under-Tension Friction Tests. *Materials* **2024**, *17*, 3631. [CrossRef] [PubMed]

183. Kuprin, A.S.; Ovcharenko, V.D.; Gilewicz, A.; Tolmachova, G.N.; Kolodiy, I.V.; Vasilenko, R.L.; Kuznetsova, T.; Lapitskaya, V.; Warcholinski, B. Structural, mechanical and tribological properties of Cr-V-N coatings deposited by cathodic arc evaporation. *Tribol. Int.* **2022**, *165*, 107246. [CrossRef]
184. Hladkyi, Y.M.; Bys', S.S.; Myl'ko, V.V. Hydrogen-Diffusion Mechanical Treatment of Structural Materials. *Mater. Sci.* **2023**, *55*, 846–853. [CrossRef]
185. Hrytsay, I.; Stupnytskyy, V.; Topchii, V. Improved method of gear hobbling computer aided simulation. *Arch. Mech. Eng.* **2019**, *66*, 475–494. [CrossRef]
186. Wang, J.; Zhang, S.; Lv, Z.; Liu, B.; Zhang, H.; Du, S.; Liu, J. Microstructure evolution and properties comparation of industrial grade-maintained 7050-T7451 plate recycled from machining chips. *J. Mater. Res. Technol.* **2023**, *25*, 6011–6026. [CrossRef]
187. Pylypenko, H.M.; Prokhorova, V.V.; Mrykhina, O.B.; Koleshchuk, O.Y.; Mushnykova, S.A. Cost Evaluation Models of R&D Products of Industrial Enterprises. *Nauk. Visnyk Natsionalnoho Hirnychoho Universytetu* **2020**, *5*, 163–170. Available online: http://nvngu.in.ua/jdownloads/pdf/2020/04/05_2020_Pylypenko.pdf (accessed on 9 July 2025). [CrossRef]
188. Prokhorova, V.; Mrykhina, O.; Koleshchuk, O.; Slastianykova, K.; Harmatiy, M. The Holistic Evaluation System of R&D Results under the Circular Economy Conditions. *East. Eur. J. Enterp. Technol.* **2023**, *6*, 15–23. [CrossRef]
189. Mysiuk, R.; Mysiuk, I.; Yuzevych, V.; Shuvar, R.; Tsyuh, S.; Pavlenchyk, N. Detection of Structure Changes in Lightweight Concrete with the Use of Machine Learning Technologies. In Proceedings of the Eighth International Congress on Information and Communication Technology (ICICT 2023), London, UK, 20–23 February 2023; Yang, X.-S., Sherratt, R.S., Dey, N., Joshi, A., Eds.; Lecture Notes in Networks and Systems. Springer: Singapore, 2023; Volume 694, pp. 359–367. [CrossRef]
190. Shpotyuk, O.I.; Balitska, V.O.; Vakiv, M.M.; Shpotyuk, L.I. Sensors of high-energy radiation based on amorphous chalcogenides. *Sens. Actuators A Phys.* **1998**, *68*, 356–358. [CrossRef]
191. Balitska, V.; Golovchak, R.; Kovalskiy, A.; Skordeva, E.; Shpotyuk, O.I. Effect of Co60 γ-irradiation on the optical properties of As–Ge–S glasses. *J. Non-Cryst. Solids* **2003**, *326–327*, 130–134. [CrossRef]
192. Balitskii, O.; Sytnyk, M.; Heiss, W. Recent developments in halide perovskite nanocrystals for indirect X-ray detection. *Adv. Mater. Technol.* **2024**, *9*, 2400150. [CrossRef]
193. Balyts'kyi, O.O. Degradation and fracture of crystals of gallium and indium selenides. *Mater. Sci.* **2003**, *39*, 561–565. [CrossRef]
194. Balyts'kyi, O.I.; Ripei, I.V.; Onyshchak, O.Y. Variations of the Impact Toughness of 12Kh1MF Steel in Operating Steam Pipelines of Thermal Power Plants. *Mater. Sci.* **2009**, *45*, 826–830. [CrossRef]
195. Xu, Y.; Liu, J.; Li, X.; Tang, C. An Investigation of Vibrations of a Flexible Rotor System with the Unbalanced Force and Time-Varying Bearing Force. *Chin. J. Mech. Eng.* **2025**, *38*, 25. [CrossRef]
196. Mokhiamar, O.; Abe, M. Experimental Verification Using a Driving Simulator of the Effect of Simultaneous Optimal Distribution of Tyre Forces for Active Vehicle Handling Control. *Proc. Inst. Mech. Eng. D* **2005**, *219*, 135–149. [CrossRef]